VLT and ACS observations of RDCS J1252.9-2927: dynamical structure and galaxy populations in a massive cluster at z=1.237 — Source link

Ricardo Demarco, Piero Rosati, Christopher Lidman, Marisa Girardi ...+26 more authors

Institutions: Johns Hopkins University, European Southern Observatory, University of Trieste, University of California, Santa Cruz ...+11 more institutions

Topics: Galaxy cluster, Brightest cluster galaxy, Velocity dispersion, Luminous infrared galaxy and Galaxy

Related papers:

- Stellar population synthesis at the resolution of 2003

- SExtractor: Software for source extraction

- Advanced Camera for Surveys Photometry of the Cluster RDCS 1252.9–2927: The Color-Magnitude Relation at z = 1.24

- Advanced Camera for Surveys Photometry of the Cluster RDCS1252.9-2927: The Color-Magnitude Relation at z=1.24

- Chandra and XMM-Newton Observations of RDCS 1252.9-2927, A Massive Cluster at z=1.24

VLT AND ACS OBSERVATIONS OF RDCS J1252.9−2927: DYNAMICAL STRUCTURE AND GALAXY POPULATIONS IN A MASSIVE CLUSTER AT $z = 1.237$[1]

R. DEMARCO,[2] P. ROSATI,[3] C. LIDMAN,[4] M. GIRARDI,[5] M. NONINO,[6] A. RETTURA,[2] V. STRAZZULLO,[3] A. VAN DER WEL,[2]
H. C. FORD,[2] V. MAINIERI,[3] B. P. HOLDEN,[7] S. A. STANFORD,[8] J. P. BLAKESLEE,[9] R. GOBAT,[3] M. POSTMAN,[10]
P. TOZZI,[6,11] R. A. OVERZIER,[2] A. W. ZIRM,[2] N. BENÍTEZ,[12] N. L. HOMEIER,[2] G. D. ILLINGWORTH,[7]
L. INFANTE,[13] M. J. JEE,[2] S. MEI,[14,15] F. MENANTEAU,[16] V. MOTTA,[17] W. ZHENG,[2]
M. CLAMPIN,[18] AND G. HARTIG[10]

ABSTRACT

We present results from an extensive spectroscopic survey, carried out with VLT FORS, and from an extensive multiwavelength imaging data set from the *HST* Advanced Camera for Surveys and ground-based facilities, of the cluster of galaxies RDCS J1252.9−2927. We have spectroscopically confirmed 38 cluster members in the redshift range $1.22 < z < 1.25$. A cluster median redshift of $z = 1.237$ and a rest-frame velocity dispersion of 747^{+74}_{-84} km s^{-1} are obtained. Using the 38 confirmed redshifts, we were able to resolve, for the first time at $z > 1$, kinematic structure. The velocity distribution, which is not Gaussian at the 95% confidence level, is consistent with two groups that are also responsible for the projected east-west elongation of the cluster. The groups are composed of 26 and 12 galaxies with velocity dispersions of 486^{+47}_{-85} and 426^{+57}_{-105} km s^{-1}, respectively. The elongation is also seen in the intracluster gas and the dark matter distribution. This leads us to conclude that RDCS J1252.9−2927 has not yet reached a final virial state. We extend the analysis of the color-magnitude diagram of spectroscopic members to more than 1 Mpc from the cluster center. The scatter and slope of non-[O II]-emitting cluster members in the near-IR red sequence is similar to that seen in clusters at lower redshift. Furthermore, most of the galaxies with luminosities greater than $\sim K_s^* + 1.5$ do not show any [O II], indicating that these more luminous, redder galaxies have stopped forming stars earlier than the fainter, bluer galaxies. Our observations provide detailed dynamical and spectrophotometric information on galaxies in this exceptional high-redshift cluster, delivering an in-depth view of structure formation at this epoch only 5 Gyr after the big bang.

Subject headings: galaxies: clusters: general — galaxies: clusters: individual (ClG J1252.9−2927)

Online material: color figures, extended figure set

1. INTRODUCTION

Clusters of galaxies are tracers of the peaks of matter density in the universe. Studying them over a wide range in redshift provides an insight into the process of mass assembly of structures through cosmic history, from galactic to Mpc scales. They are suitable laboratories in which to study galaxy populations, providing clues to better understand the effects of the local environment on galaxy properties and galaxy evolution. Cluster X-ray luminosity and temperature indicate the existence of massive systems ($M > 10^{14}$ $M_\odot$) already when the universe was half its present age (Jeltema et al. 2001; Maughan et al. 2003, 2004; Rosati et al. 2004; Mullis et al. 2005). While some of these clus-

ters have a relaxed X-ray morphology by $z \sim 0.8$ (Maughan et al. 2004), others show clear signatures of being still in a formation stage, as indicated by their filamentary morphology and the presence of substructure (Gioia et al. 1999, 2004; Demarco et al. 2005; Girardi et al. 2005; Tanaka et al. 2006).

The dense cluster environment has a profound effect on the properties of the cluster galaxies. Most notably, early-type galaxies are more prevalent in clusters than in low-density field environments (Dressler 1980), and this morphology-density relation has existed since $z \sim 1$ (Dressler et al. 1997; Smith et al. 2005; Postman et al. 2005). The existence of the morphology-density relation suggests that the properties of the stellar populations of galaxies also depend on their environment, which is corroborated by the relation between star formation history, color, and environment (Balogh et al. 1998; Helsdon & Ponman 2003;

[1] Based on observations carried out with the ESO VLT under programs 166.A-0701, 69.A-0683, 73.A-0832, and 76.A-0889.

[2] Department of Physics and Astronomy, Johns Hopkins University, Baltimore, MD 21218; corresponding author: demarco@pha.jhu.edu.

[3] ESO-European Southern Observatory, Karl-Schwarzschild-Strasse 2, D-85748, Garching bei München, Germany.

[4] ESO-European Southern Observatory, Alonso de Cordova 3107, Casilla 19001, Santiago, Chile.

[5] Dipartimento di Astronomia, Università degli Studi di Trieste; and INAF-Osservatorio Astronomico di Trieste, via Tiepolo 11, 34131 Trieste, Italy.

[6] INAF-Osservatorio Astronomico di Trieste, via G.B. Tiepolo 11, 34131 Trieste, Italy.

[7] UCO/Lick Observatory, University of California, Santa Cruz, 1156 High Street, Santa Cruz, CA 95065.

[8] University of California, Davis, CA 95616; and Institute of Geophysics and Planetary Physics, Lawrence Livermore National Laboratory, Livermore, CA 94551.

[9] Department of Physics and Astronomy, Washington State University, Pullman, WA 99164-2814.

[10] Space Telescope Science Institute, 3700 San Martin Drive, Baltimore, MD 21218.

[11] NFN, National Institute for Nuclear Physics, Trieste, Italy.

[12] Instituto de Astrofísica de Andalucía (CSIC), Camino Bajo de Huétor 50, Granada 18008, Spain.

[13] Departamento de Astronomía y Astrofísica, Pontificia Universidad Católica de Chile, Casilla 306, 22 Santiago, Chile.

[14] University of Paris Diderot, 75205 Paris Cedex 13, France.

[15] GEPI, Observatoire de Paris, Section de Meudon, 92195 Meudon Cedex, France.

[16] Department of Physics and Astronomy, Rutgers, the State University of New Jersey, Piscataway, NJ 08854-8019.

[17] Departamento de Física y Meteorología, Universidad de Valparaíso, Avda. Gran Bretaña 1111, Valparaíso, Chile.

[18] NASA Goddard Space Flight Center, Code 680, Greenbelt, MD 20771.

Kauffmann et al. 2004; Wake et al. 2005; Postman et al. 2005; Homeier et al. 2006a; Thomas & Katgert 2006).

Measurements of the evolution of the mass-to-light ratio of massive cluster early-type galaxies have demonstrated that their stellar populations were largely formed at $z > 2$ (e.g., van Dokkum & Stanford 2003; Holden et al. 2005). The slow evolution of the color-magnitude relation (e.g., Blakeslee et al. 2003b, 2006; Holden et al. 2004; Mei et al. 2006a, 2006b; Homeier et al. 2006b) shows that this is the case for early-type galaxies well below the characteristic luminosity, although there seems to be a lack of faint, red galaxies at redshifts higher than $z \sim 0.5$ (Tanaka et al. 2005). Remarkably, massive field early-type galaxies have been shown to be not much younger, in terms of their stellar populations, than cluster early-type galaxies with the same mass (van der Wel et al. 2005; Treu et al. 2005; van Dokkum & van der Marel 2006). This raises the question whether galaxy mass or environment is the most important driver of galaxy evolution.

Most of our knowledge of cluster evolution comes from observations at redshift lower than unity and a few sparse data sets at $z = 1–1.3$. Observing galaxy clusters at $z > 1$ is difficult, and only a small number of galaxy clusters at such a high redshift have been confirmed to date (Stanford et al. 1997, 2002, 2005, 2006; Rosati et al. 1999, 2004; Hashimoto et al. 2004; Mullis et al. 2005; Brodwin et al. 2006; Elston et al. 2006). With the primordial activity of cluster and massive galaxy formation happening at $z \gtrsim 1$, the observations of systems at those redshifts offer the possibility of learning more about their physical properties at an epoch when baryons are first being assembled into gravitationally bound systems within massive dark matter halos. One of those high-redshift clusters, RDCS J1252.9−2927 (Rosati et al. 2004), is a massive X-ray luminous system at $z = 1.24$ selected from the *ROSAT* Deep Cluster Survey (RDCS; Rosati et al. 1998), which has been the center of an intensive multiwavelength campaign in the past 5 years.

RDCS J1252.9−2927 ($\alpha_{J2000} = 12^h52^m48^s$, $\delta_{J2000} = −29°27'00''$) was discovered in the 15.7 ks *ROSAT* PSPC field with ID WP300093 at an off-axis angle of $13.9'$ with 31 net counts, corresponding to a flux of $(2.5 \pm 0.9) \times 10^{-14}$ ergs cm^{-2} s^{-1} in the 0.5–2 keV band. *I*-band imaging (30 minute exposure), obtained with the Prime Focus camera at the CTIO 4 m telescope in February 1997, revealed a faint ($I \simeq 21.7$) galaxy pair very close to the X-ray centroid position. In November 1998, *J*- and K_s-band imaging obtained with SofI (Moorwood et al. 1998) on the ESO New Technology Telescope (NTT) showed a clear overdensity of red galaxies with $J − K_s \simeq 1.9$, typical of early-type galaxies at $z > 1$ (Lidman et al. 2004).

X-ray imaging with *Chandra* and *XMM-Newton* has been obtained, allowing a complete modeling of the X-ray surface brightness of the cluster together with an unprecedented accuracy in the estimation of its temperature, metallicity, and dynamical mass (Rosati et al. 2004). RDCS J1252.9−2927 is a massive structure with a luminosity of $L_X(bol) = (6.6 \pm 1.1) \times 10^{44}$ ergs s^{-1} ($H_0 = 70$ km s^{-1} Mpc^{-1}, $\Omega_m = 0.3$, and $\Omega_\lambda = 0.7$) measured within an aperture of $60''$ (500 kpc) radius and a total mass of $M = (1.9 \pm 0.3) \times 10^{14}$ $M_\odot$ within a R_{500} radius[19] of 536 ± 40 kpc (Rosati et al. 2004). Its intracluster medium (ICM) is characterized by a temperature $T_X = 6.0^{+0.7}_{-0.5}$ keV and a metallicity $Z = 0.36^{+0.12}_{-0.10}$ $Z_\odot$ (Rosati et al. 2004), and the surface brightness profile shows a discontinuity typical of cold fronts systems found in *Chandra* observations of low-redshift clusters.

High angular resolution optical observations of the cluster with the Advanced Camera for Surveys (ACS; Ford et al. 1998) on the *Hubble Space Telescope* (*HST*) delivered unprecedented morphological information on the cluster galaxy populations as well as accurate photometry (Blakeslee et al. 2003b). Additional ground-based photometry in the near-IR (Lidman et al. 2004) has been obtained with ISAAC (Infrared Spectrometer and Array Camera) on the ESO Very Large Telescope (VLT), while *Spitzer* IRAC observations of RDCS J1252.9−2927 (S. A. Stanford et al., in preparation) have made it possible to sample the rest-frame near-IR light of the cluster.

During the past few years we have carried out an extensive spectroscopic survey of RDCS J1252.9−2927 with the ESO VLT, with the aim of confirming a large fraction of the cluster population. This effort has yielded the most complete spectroscopic data set so far on this cluster. In this paper we present the results from this ESO VLT/FORS (Focal Reducer and low-dispersion Spectrograph) spectroscopic program in combination with ACS and VLT/ISAAC imaging data. This investigation aims to spectroscopically identify the cluster galaxy populations in order to study the cluster dynamics from galaxy kinematics and the spectrophotometric properties of cluster members. Unless otherwise indicated, we assume a ΛCDM cosmology with $H_0 = 70$ km s^{-1} Mpc^{-1}, $\Omega_M = 0.3$, and $\Omega_\Lambda = 0.7$.

2. DATA SET AND DATA REDUCTION

2.1. *ACS and Ground-based Imaging Data*

Imaging observations of RDCS J1252.9−2927 in the optical have been carried out from the ground and from space. The ACS Wide Field Camera (WFC) on *HST* was used to obtain imaging with the F775W and F850LP filters (hereafter i_{775} and z_{850}, respectively), as part of a guaranteed time observation program (ObsID 9290). Three orbits in i_{775} and five orbits in z_{850} were completed during 2002 May and June, distributed in a 2×2 mosaic pattern. The pointings overlapped about $1'$, producing exposures of 12 orbits in i_{775} and 20 orbits in z_{850} of the cluster core. A more detailed description of the ACS data on RDCS J1252.9−2927 is presented in Blakeslee et al. (2003b).

The ground-based optical data were collected with FORS2 (Appenzeller & Rupprecht 1992) on the VLT, under ESO program 169.A-0458(A). The imaging data in the *B*, *V*, and *R* bands[20] were obtained between 2003 March 1 and March 3, in very good seeing conditions. The co-added images have FWHM of $0.66''$ in the *B* band, $0.60''$ in the *V* band, and $0.56''$ in the *R* band. The photometric calibration was done using the many Landolt field stars that were observed during the same nights. The images have been corrected for instrumental response, bias, and flat, in a standard manner. All images were photometrically aligned by using about 100 bright but unsaturated stars in the field, which showed that the nights were indeed photometric. The images were astrometrically flattened and then finally co-added. As a further check, the same point sources used for the single-image photo alignment were compared with FORS1 data acquired in May 1999, in the same *B*, *V*, and *R* bands. The mean differences in magnitude for the selected objects were $−0.006 \pm 0.030$ in *B* and 0.015 ± 0.021 in *V*. In the *R* band, a $V − R$ color term correction was found giving a mean difference of 0.002 ± 0.032.

Ground-based near-IR imaging observations of RDCS J1252.9−2927 were taken with ISAAC (Moorwood et al. 1999) on the

---

[19] R_Δ is defined as the radius within which the mean density is Δ times the critical density of the universe at a given redshift.

[20] The *B*, *V*, and *R* bands correspond to the B_BESSEL, V_BESSEL and R_SPECIAL (FORS2) or R_BESSEL (FORS 1) filters, respectively.

ESO VLT and are described in Lidman et al. (2004) . In the central regions of the cluster the data reach limiting magnitudes (5 σ limit over a 0.9″ diameter aperture) of 26.5 (AB) and 26.0 (AB) in the J and K_s bands, respectively. Since then, these data have been reprocessed to optimize image quality and to facilitate the computation of aperture corrections over the entire region covered by near-IR observations. The image quality in the reprocessed images varies from 0.32″ to 0.43″. The FWHM of point sources in a single tile is relatively constant, and this makes it simpler to compute these aperture corrections, whereas the FWHM of point sources in the mosaic varies from tile to tile. Hence, rather than combining the images into a single mosaic, each tile was processed and analyzed separately. This means that some objects appear multiple times, as there is considerable overlap between different tiles. To handle this, we create catalogs for each tile, and if a source is in more than one catalog, we average the result. We also compute an error from the different measurements and compare it to the error computed in SExtractor. If the source is in only one catalog, we use the error computed in SExtractor; otherwise we use either the SExtractor error or the error derived from the multiple measurements, whichever is largest. Magnitudes are measured in 10 pixel diameter apertures (∼1.5″) and then corrected to larger apertures (4″ diameter) using stars in each tile to compute aperture corrections.

2.2. *The Photometric Catalog*

A first multicolor catalog was built out of the above data sets. This catalog contained the photometry computed from the ISAAC mosaic as described in Lidman et al. (2004) without including the more recently reprocessed ISAAC photometry (see § 2.1). We note that the original ISAAC photometry in Lidman et al. (2004) and the reprocessed one presented here (see below) are in good agreement with each other, showing median differences of 0.002 in K_s and 0.007 in J_s with dispersion (σ) values of 0.064 and 0.033, respectively. The ACS, FORS2, and ISAAC images have different PSF FWHM. In order to avoid source blending due to a plain smoothing of the best-seeing images to match the worst one, we adopt a different strategy to correct for these different PSFs. Using the same bright pointlike sources as before (see § 2.1), we construct growth curves. We then computed the aperture magnitude for all ground-based and ACS images using an aperture of 1.5″ diameter. An aperture correction from 1.5″ to 4″ diameter is first computed using point sources, and then applied to all sources in the optical (ACS and FORS2) and near-IR (ISAAC) bands. Although this aperture correction is not strictly equivalent to the smoothing technique, we have checked, using the ACS data, that the two approaches give consistent results. The main advantage of using this approach instead of the smoothing one in this analysis is that we avoid significant source blending, especially in the central region of the cluster. This catalog was used to select candidates for spectroscopy while preparing most of the FORS2 masks.

The final photometric catalog published in this work and showing only spectroscopic cluster members is presented in Table 3. It contains the *B*-, *V*-, and *R*-band photometry from FORS2, the i_{775}- and z_{850}-band photometry from ACS, and the newly processed J_s and K_s ISAAC photometry, all of them as described above. The magnitudes are aperture corrected to a radius of 2″ and are in the AB system (Oke 1974). To transform our photometry from the Vega system to the AB system, we recomputed AB corrections adopting the latest available Vega spectrum. The AB corrections for the *B*, *V*, *R*, J_s, *J*, and K_s filters are −0.088, 0.052, 0.244, 0.968, 0.964, and 1.899 respectively. For the i_{775} and z_{850} filters

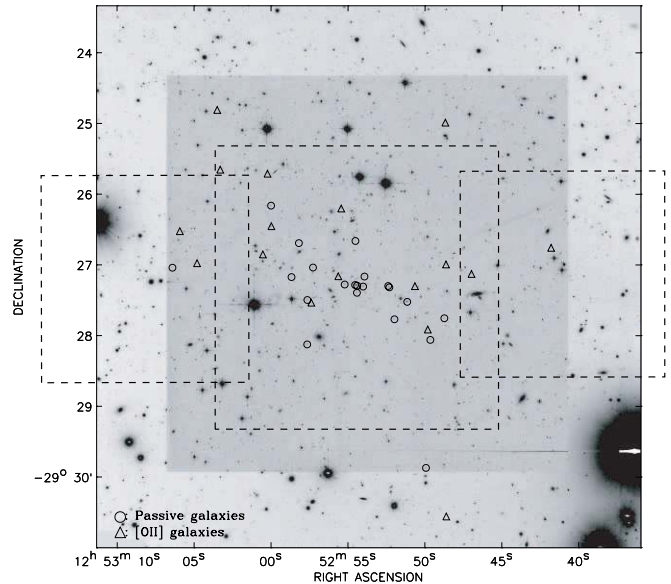
Fig. 1.—Projected distribution of cluster members on the sky (north is up and east is to the left). Circles are non-star-forming galaxies, and triangles are galaxies showing [O II] (λ3727) in their spectrum. The background image corresponds to the FORS2 coverage in *BVR*, the darker image corresponds to the z_{850} ACS data, and the dashed lines show the field covered by ISAAC. The overall shape of the distribution of confirmed galaxy members is clearly elongated in the east-west direction.

we use AB correction values of 0.401 and 0.569, respectively (Blakeslee et al. 2003a). Values in Table 3 are corrected for Galactic extinction. In order to take into account the Galactic reddening in our analyses, we used the extinction maps of Schlegel et al. (1998). The corrections for the *B*, *V*, *R*, i_{775}, z_{850}, J_s, and K_s bands are 0.323, 0.248, 0.200, 0.145, 0.127, 0.067 and 0.027, respectively. Near-IR magnitudes presented in Figures 2 and 14 are placed on the 2MASS *J*, K_s system (Carpenter 2001; Cohen et al. 2003). The corresponding transformation, including the Galactic reddening correction, is given by:

$$(J - K_s)_{2MASS} = 1.038(J_s - K_s)_{ISAAC} - 0.048 \qquad (1)$$

and

$$K_{s,\,2MASS} = K_{s,\,ISAAC} - 0.028. \qquad (2)$$

Unless otherwise stated, magnitudes presented throughout this paper are in the AB system.

2.3. *Photometric Selection*

The above photometric information was used to compute photometric redshifts (Benítez 2000) for all the objects within the field of view (FoV) covered by the ISAAC mosaic (Lidman et al. 2004). This region was chosen in order to have optical ACS, optical FORS2, and near-IR ISAAC photometry available (see Fig. 1) to compute photometric redshifts. The set of galaxy templates for the photometric redshift calculations is presented in Benítez et al. (2004). Photometric redshifts together with color-color diagrams were used to select candidate galaxies for spectroscopy. In our first spectroscopic campaign, galaxies with $K_s <$ 21, $J_s - K_s < 2.1$, and $R - K_s > 3$ were targeted. This selection of the spectroscopic sample, indicated by the dashed lines in
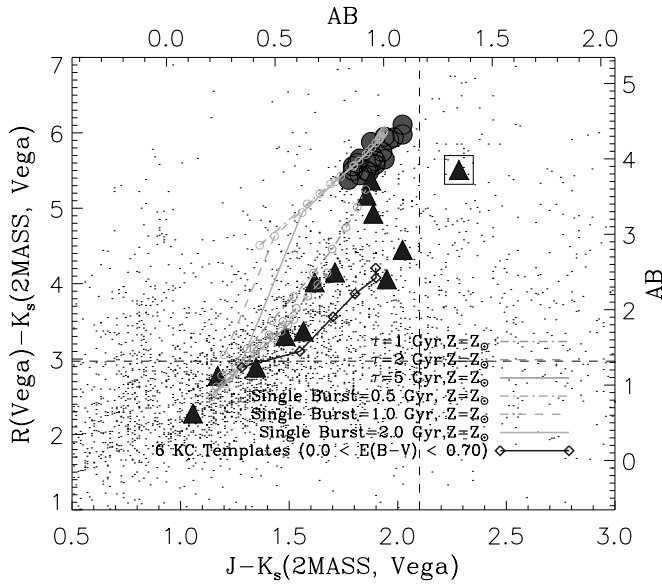
FIG. 2.—Color-color selection of the spectroscopic sample. Galaxies with $K_s < 21$, $J − K_s < 2.1$, and $R − K_s > 3$ were targeted. The different color tracks correspond to different evolutionary models, computed with Bruzual & Charlot's code, and to 6 KC templates with different $E(B − V)$ color excess (see text for details). The square indicates the spectroscopically confirmed cluster AGN (ID 174). Filled circles indicate passive members, while filled triangles indicate emission-line [O II] (λ3727) members. Small dots are objects in our full photometric catalog. [*See the electronic edition of the Journal for a color version of this figure.*]

Figure 2, minimizes the pollution by field galaxies, although it can be slightly biased against very red ($J_s − K_s \gtrsim 2.2$) cluster galaxies. This primary selection was complemented by another one on the $V − I$ versus $I − z_{850}$ plane in order to improve the selection of Balmer-break and [O II] (λ3727) galaxies. The color tracks in Figure 2 correspond to different evolutionary models, computed with the BC03 code (Bruzual & Charlot 2003), reproducing galaxy colors observed at $z = 1.237$ for different ages (from 1 to 5 Gyr). These models were employed together with the avail-

able multicolor information to guide the selection of targets. The orange lines represent single burst, solar metallicity models with burst durations of 0.5 Gyr (*dot-dashed*), 1.0 Gyr (*dashed*), and 2.0 Gyr (*solid*). The green lines represent exponentially declining star formation rate (SFR), solar metallicity models with characteristic times of $\tau = 1$ Gyr (*dot-dashed*), $\tau = 2$ Gyr (*dashed*), and $\tau = 5$ Gyr (*solid*). Model points, indicated by small open circles, are spaced by 0.5 Gyr in age and are in the ISAAC system. The blue line corresponds to six starburst galaxy templates from Kinney et al. (1996), hereafter KC templates, spanning the mean color excess range $0.0 < E(B − V) < 0.70$ and marked by open diamonds. In subsequent campaigns, we took advantage of photometric redshifts in the range $1.1 \lesssim z_{phot} \lesssim 1.3$ as they became available.

2.4. *VLT Spectroscopy*

A total of 15 masks were designed to be observed with FORS1 and FORS2. The data were obtained as part of an ESO Large Program (LP-166.A-0701) and two subsequent ESO proposals (69.A-0683 and 073.A-0832). The spectroscopic observations started in 2000 March and ended in 2004 April. The first mask was observed in MOS mode with FORS1 and the 300I grism, whereas the other 14 masks were all observed with FORS2. Spectroscopy with FORS2 was carried out with both the 300I and 150I grisms. All the masks designed for MXU spectroscopy were observed with the 300I grism, while all but one MOS mode observations were carried out with the 150I grism. The slit width for MXU observations was set to $1''$, while the MOS masks were designed with slit widths of $1.4''$ and $1.7''$. A summary of our spectroscopic observations is presented in Table 1 and more detailed information about the MOS and MXU modes as well as the grism characteristics are given in Demarco et al. (2005). From 2002 October on, the observations were carried out with a CCD mosaic composed of two 2k × 4k MIT/LL detectors with increased sensitivity (∼30%) in the red, allowing us to obtain a better success rate than previous observations with the old FORS2 CCD. The data were reduced following the same procedure described in Demarco et al. (2005).

TABLE 1
SUMMARY OF THE VLT SPECTROSCOPIC DATA OBTAINED FOR RDCS J1252.9−2927

Mask Name	Date	Telescope	Instrument[a]	Grism/Filter[b]	Exposure Time (hr)	Mask
m1	2001 Mar	UT2	FORS2	300I/OG590	4.9	MXU
m2	2001 Mar	UT2	FORS2	300I/OG590	4.0	MXU
m3	2001 Mar	UT2	FORS2	300I/OG590	0.9	MXU
m3	2001 Apr	UT2	FORS2	300I/none	4.5	MXU
m4	2001 Mar	UT2	FORS2	300I/OG590	1.7	MOS
m4	2001 Mar	UT2	FORS2	150I/GG435	1.4	MOS
m5	2001 Mar	UT2	FORS2	150I/GG435	1.3	MOS
m6	2001 Apr	UT2	FORS2	300I/none	4.5	MXU
m7	2001 Apr	UT2	FORS2	150I/none	2.0	MOS
m8	2001 Apr	UT2	FORS2	150I/none	2.0	MOS
m9	2001 Apr	UT2	FORS2	150I/none	1.0	MOS
m10	2001 Apr	UT2	FORS2	300I/none	2.5	MXU
m11	2002 Oct	UT4	FORS2*	300I/none	6.5	MXU
m12	2003 Feb	UT4	FORS2*	300I/none	3.7	MXU
m13	2003 Feb	UT4	FORS2*	300I/none	3.0	MXU
m14	2004 Apr	UT4	FORS2*	300I/none	4.7	MXU
m15	2004 Apr	UT4	FORS2*	300I/none	4.7	MXU

[a] The asterisk (*) indicates observations carried out with the mosaic of two 2k × 4k MIT CCDs.
[b] Grism/Filter corresponds to the grism/order sorting filter combination used.

TABLE 2
Spectroscopically Confirmed Cluster Members

ID (1)	R.A. (2)	Decl. (3)	z (4)	R (5)	Spectral Features[a] (6)	Emission Line Flag (7)	Flux [O II] (8)	EW [O II] (9)	SFR (10)
137	12 52 57.65	−29 28 07.5	1.2475 ± 0.0004	2.37	Mg I; Ca II (H+K); D4000; Hδ	0	...	...	...
149	12 52 49.65	−29 28 03.7	1.2382 ± 0.0003	3.45	Mg I; Ca II (H+K); D4000; Hδ	0	...	...	...
174	12 52 49.82	−29 27 54.9	1.2382 ± 0.0002	4.73	[O II]	1	1.25 ± 0.04	−596 ± 528	0.7 ± 0.2
205	12 52 51.98	−29 27 46.2	1.2318 ± 0.0003	4.11	Mg I; Ca II (H+K); D4000; Ca I	0	...	...	...
206	12 52 48.74	−29 27 45.3	1.2353 ± 0.0003	3.11	H8; Mg I; H6; Ca II (H+K); D4000	0	...	...	...
247	12 52 51.15	−29 27 31.4	1.2351 ± 0.0002	5.79	H8; H6; Ca II (H+K); D4000; Hδ; Ca I	0	...	...	...
248	12 52 57.39	−29 27 32.1	1.2322 ± 0.0001	4.91	[O II]; Ca II (H); Ca I	1	0.54 ± 0.20	−63 ± 24	0.3 ± 0.2
265	12 52 57.64	−29 27 29.8	1.2358 ± 0.0004	1.98	H8; Ca II (K); D4000	0	...	...	...
282	12 52 54.42	−29 27 23.7	1.2472 ± 0.0004	1.99	Ca II (H+K); D4000; Ca I	0	...	...	...
289	12 52 54.54	−29 27 17.1	1.2378 ± 0.0006	2.23	H9; D4000; Ca I	0	...	...	...
291	12 52 54.41	−29 27 17.7	1.2343 ± 0.0003	5.21	Fe I; H9; H8; Ca II (H+K); D4000; Hδ	0	...	...	...
294	12 52 52.31	−29 27 19.1	1.2455 ± 0.0003	4.13	Mg I; Ca II (H+K); D4000; Ca I	0	...	...	...
304	12 52 54.02	−29 27 18.5	1.2384 ± 0.0003	3.96	Mg I; H6; Ca II (H+K); D4000; Ca I	0	...	...	...
309	12 52 50.66	−29 27 18.1	1.2312 ± 0.0002	3.92	[O II]; H6; Ca II (H+K); Hδ; Ca I	1	0.85 ± 0.20	−32 ± 8	0.5 ± 0.2
310	12 52 52.39	−29 27 18.0	1.2342 ± 0.0003	3.69	Fe I; He I; H8; Mg I; H6; Ca II (H+K); D4000; Ca I	0	...	...	...
313	12 52 55.22	−29 27 16.7	1.2455 ± 0.0006	3.58	Fe I; H10; Mg I; Ca II (H+K); D4000; Ca I	0	...	...	...
330	12 52 58.67	−29 27 10.4	1.2297 ± 0.0003	4.09	He I; H9; H8; Mg I; H6; Ca II (H+K); D4000; Hδ	0	...	...	...
338	12 52 53.93	−29 27 09.9	1.2312 ± 0.0003	4.09	Fe I; He I; H8; Mg I; Ca II (H+K); D4000; Hδ; Ca I	0	...	...	...
339	12 52 55.63	−29 27 09.7	1.2274 ± 0.0002	3.43	[O II]; H9; H8	1	1.78 ± 0.20	−34 ± 4	1.0 ± 0.4
345	12 52 46.98	−29 27 07.7	1.2379 ± 0.0004	1.00	H10; Mg I; [O II]; D4000	1	5.00 ± 2.85	−40 ± 23	2.9 ± 2.4
366	12 52 48.64	−29 26 59.7	1.2371 ± 0.0001	6.92	[O II]	1	0.08 ± 0.03	−106 ± 36	0.05 ± 0.03
367	12 52 57.27	−29 27 02.3	1.2295 ± 0.0003	6.92	Mg I; Ca II (H+K); D4000	0	...	...	...
370	12 53 06.41	−29 27 02.4	1.2373 ± 0.0010	1.24	Fe I; H10; Mg I; Ca II (H+K); D4000	0	...	...	...
407	12 53 00.00	−29 26 09.8	1.2354 ± 0.0002	5.92	H8; Mg I; Ca II (H+K); D4000; Hδ; Ca I	0	...	...	...
419	12 52 41.81	−29 26 45.5	1.2338 ± 0.0001	5.07	[O II]	1	1.71 ± 0.72	−79 ± 33	1.0 ± 0.7
432	12 52 58.19	−29 26 41.6	1.2416 ± 0.0003	4.19	H10; Mg I; H6; Ca II (H+K); D4000	0	...	...	...
442	12 52 54.52	−29 26 39.8	1.2306 ± 0.0003	3.63	He I; Mg I; H6; Ca II (H+K); D4000	0	...	...	...
445	12 52 59.98	−29 26 27.2	1.2400 ± 0.0004	2.94	[O II]; H10; Mg I; H6; Ca II (H+K)	1	1.33 ± 0.27	−30 ± 6	0.8 ± 0.4
515	12 52 55.44	−29 26 12.2	1.2402 ± 0.0001	5.26	He I; H9; Ca II (H+K); [O II]	1	0.91 ± 0.20	−55 ± 12	0.5 ± 0.3
619	12 53 00.23	−29 25 42.7	1.2432 ± 0.0004	1.38	[O II]; Ca I	1	6.70 ± 1.56	−28 ± 7	3.9 ± 1.9
726	12 53 05.93	−29 26 31.4	1.2273 ± 0.0001	2.79	[O II]	1	3.33 ± 0.65	−130 ± 25	1.9 ± 0.9
2065	12 53 03.30	−29 25 39.3	1.2327 ± 0.0001	15.54	[O II]	1	5.09 ± 0.51	−145 ± 15	3.0 ± 1.0
3159	12 53 00.53	−29 26 51.2	1.2459 ± 0.0003	1.87	[O II]; H10; H9; H8	1	0.56 ± 0.14	−30 ± 7	0.3 ± 0.2
6301	12 53 03.50	−29 24 48.6	1.2408 ± 0.0001	7.36	[O II]	1	4.68 ± 1.16	−80 ± 20	2.7 ± 1.4
6306	12 52 48.68	−29 24 59.3	1.2380 ± 0.0001	4.45	[O II]; H9; H8; Mg I; H6; Ca II (H+K); Hδ	1	3.20 ± 0.47	−44 ± 6	1.9 ± 0.7
7001	12 52 48.61	−29 30 33.5	1.2368 ± 0.0003	2.49	Fe I; He I; [O II]; H9; H8; Mg I; H6; Ca II (H+K); Hδ	1	0.32 ± 0.09	−25 ± 7	0.2 ± 0.1
7005	12 52 49.93	−29 29 52.3	1.2416 ± 0.0006	3.28	He I; H10; H8; Mg I; H6; Ca II (H+K); D4000; Hδ	0	...	...	...
9000	12 53 04.81	−29 26 58.6	1.2438 ± 0.0001	3.20	[O II]	1	0.30 ± 0.01	−100 ± 42	0.2 ± 0.1

Notes.—Cols. (2), (3): R.A. and decl. (J2000). Units of right ascension are hours, minutes, and seconds, and units of declination are degrees, arcminutes, and arcseconds. Col. (4): Redshift and its formal error as obtained from the cross-correlation. Col (5): Correlation coefficient, R, as defined in Tonry & Davis (1979). Col. (6): Most prominent spectral features identified in the spectrum. Col. (7): Emission line flag assigned to the object. A value of 0 corresponds to galaxies without emission lines, and a value of 1 corresponds to galaxies with narrow emission lines. Cols. (8)–(10): Integrated [O II] line flux (in $\times 10^{-17}$ ergs s^{-1} cm^{-2}), the [O II] line equivalent width (EW; in Å), and the star-formation rate (SFR), in $M_\odot$ yr^{-1}.

[a] Most prominent spectral features: Fe I ($\lambda 3581$), He I ($\lambda 3614$), [O II] ($\lambda 3727$), H10 ($\lambda 3750$), H9 ($\lambda 3770$), H8 ($\lambda 3799$), Mg I($\lambda 3834$), H6 ($\lambda 3889$), the Ca II lines H ($\lambda 3934$) and K ($\lambda 3969$), the decrement at 4000 Å (D4000), Hδ ($\lambda 4102$), and Ca I ($\lambda 4227$).

TABLE 3
Photometric Catalog of Spectroscopically Confirmed Cluster Members

ID	K_s^{tot}	$B - V$	$V - R$	$V - i_{775}$	$R - K_s$	$i_{775} - z_{850}$	$J_s - K_s$	T Type
137	20.97 ± 0.01	0.60 ± 0.15	1.42 ± 0.08	2.56 ± 0.06	3.72 ± 0.05	0.93 ± 0.02	0.76 ± 0.02	−5
149	21.01 ± 0.01	1.21 ± 0.31	1.68 ± 0.09	2.80 ± 0.08	3.84 ± 0.05	0.90 ± 0.02	0.84 ± 0.02	−2
174	20.98 ± 0.02	0.27 ± 0.10	0.51 ± 0.08	1.37 ± 0.06	3.85 ± 0.06	0.74 ± 0.05	1.25 ± 0.03	8
205	21.03 ± 0.02	1.24 ± 0.26	1.00 ± 0.08	2.20 ± 0.06	3.94 ± 0.06	0.92 ± 0.02	0.80 ± 0.02	−2
206	20.96 ± 0.01	0.52 ± 0.15	1.32 ± 0.08	2.29 ± 0.07	3.78 ± 0.05	0.98 ± 0.03	0.81 ± 0.02	−5
247	19.53 ± 0.01	1.22 ± 0.11	1.26 ± 0.04	2.38 ± 0.03	4.00 ± 0.03	0.99 ± 0.01	0.82 ± 0.01	−5
248	21.68 ± 0.07	0.21 ± 0.08	0.32 ± 0.06	0.96 ± 0.04	2.79 ± 0.06	0.68 ± 0.02	1.00 ± 0.04	8
265	21.02 ± 0.01	0.79 ± 0.15	1.04 ± 0.07	2.15 ± 0.05	3.82 ± 0.05	0.97 ± 0.02	0.85 ± 0.02	−2
282	20.60 ± 0.05	1.02 ± 0.20	1.13 ± 0.08	2.31 ± 0.06	4.28 ± 0.06	0.95 ± 0.01	0.96 ± 0.02	−5
289	19.54 ± 0.04	0.80 ± 0.12	1.45 ± 0.06	2.49 ± 0.04	4.02 ± 0.04	0.96 ± 0.01	0.87 ± 0.01	−5
291	19.22 ± 0.03	1.11 ± 0.11	1.28 ± 0.04	2.34 ± 0.03	4.09 ± 0.03	0.96 ± 0.01	0.91 ± 0.01	−5
294	20.31 ± 0.05	1.08 ± 0.13	1.21 ± 0.06	2.23 ± 0.04	3.97 ± 0.04	0.93 ± 0.01	0.89 ± 0.01	−5
304	19.75 ± 0.11	1.28 ± 0.18	1.45 ± 0.06	2.58 ± 0.05	4.25 ± 0.04	0.97 ± 0.01	0.94 ± 0.02	−5
309	20.97 ± 0.01	0.66 ± 0.09	0.78 ± 0.05	1.47 ± 0.03	3.27 ± 0.04	0.94 ± 0.01	0.87 ± 0.02	−2
310	20.54 ± 0.03	1.08 ± 0.15	0.99 ± 0.06	2.00 ± 0.04	3.99 ± 0.05	0.89 ± 0.01	0.91 ± 0.02	−5
313	20.32 ± 0.01	99	1.52 ± 0.09	2.74 ± 0.07	4.45 ± 0.05	1.02 ± 0.01	1.00 ± 0.01	−5
330	20.85 ± 0.01	0.69 ± 0.16	1.39 ± 0.08	2.55 ± 0.05	3.94 ± 0.05	0.88 ± 0.02	0.86 ± 0.02	−5
338	20.93 ± 0.02	1.18 ± 0.22	1.28 ± 0.08	2.33 ± 0.06	3.92 ± 0.05	0.92 ± 0.01	0.88 ± 0.03	−5
339	20.85 ± 0.01	0.04 ± 0.04	0.20 ± 0.04	0.63 ± 0.02	2.40 ± 0.03	0.64 ± 0.01	0.92 ± 0.02	8
345	20.76 ± 0.01	0.33 ± 0.10	1.07 ± 0.06	2.09 ± 0.04	3.71 ± 0.04	0.99 ± 0.01	0.85 ± 0.02	3
366	22.26 ± 0.08	0.17 ± 0.04	0.14 ± 0.04	0.65 ± 0.02	1.71 ± 0.05	0.52 ± 0.01	0.55 ± 0.06	3
367	20.97 ± 0.04	0.69 ± 0.14	1.05 ± 0.07	2.03 ± 0.05	3.90 ± 0.05	0.95 ± 0.02	0.78 ± 0.02	−2
370	21.33 ± 0.06	99	1.76 ± 0.14	3.07 ± 0.12	4.32 ± 0.11	1.00 ± 0.03	1.00 ± 0.14	−1
407	20.21 ± 0.01	1.13 ± 0.21	1.62 ± 0.07	2.78 ± 0.06	4.29 ± 0.04	0.99 ± 0.02	0.92 ± 0.01	−2
419	21.89 ± 0.08	0.23 ± 0.06	0.32 ± 0.05	0.83 ± 0.04	2.49 ± 0.14	0.69 ± 0.02	0.71 ± 0.19	8
432	21.47 ± 0.01	0.69 ± 0.20	0.91 ± 0.11	2.35 ± 0.08	4.22 ± 0.08	0.81 ± 0.04	0.86 ± 0.03	−5
442	21.26 ± 0.05	0.39 ± 0.17	1.40 ± 0.09	2.59 ± 0.07	3.84 ± 0.06	0.91 ± 0.01	0.77 ± 0.02	−5
445	20.31 ± 0.01	0.44 ± 0.07	0.83 ± 0.05	1.63 ± 0.04	3.51 ± 0.04	0.91 ± 0.02	0.84 ± 0.01	−5
515	22.07 ± 0.11	0.03 ± 0.04	0.24 ± 0.04	0.70 ± 0.02	1.65 ± 0.06	0.46 ± 0.01	0.48 ± 0.09	8
619	21.65 ± 0.02	0.20 ± 0.06	0.27 ± 0.05	0.93 ± 0.04	2.36 ± 0.05	0.70 ± 0.04	0.61 ± 0.04	6
726	23.15 ± 0.16	0.06 ± 0.06	0.26 ± 0.05	0.65 ± 0.04	1.12 ± 0.43	0.33 ± 0.04	0.18 ± 0.52	−
2065	22.78 ± 0.05	0.09 ± 0.04	0.20 ± 0.04	0.58 ± 0.03	1.23 ± 0.07	0.43 ± 0.03	0.34 ± 0.08	8
3159	23.87 ± 0.09	0.55 ± 0.05	0.23 ± 0.04	0.52 ± 0.03	0.62 ± 0.12	0.14 ± 0.03	0.07 ± 0.13	0
6301	99	0.00 ± 0.04	0.22 ± 0.04	0.48 ± 0.04	99	0.43 ± 0.04	99	0
6306	99	0.29 ± 0.07	0.63 ± 0.05	1.22 ± 0.04	99	0.85 ± 0.03	99	1
7001	99	99	99	99	99	99	99	−
7005	99	1.06 ± 0.21	1.16 ± 0.08	2.14 ± 0.07	99	0.88 ± 0.04	99	−1
9000	99	0.23 ± 0.11	0.36 ± 0.09	0.87 ± 0.08	99	0.61 ± 0.08	99	8

Notes.— The galaxy ID in the catalog is given in the first column. Magnitudes in the AB system, corrected for galactic reddening, and the corresponding errors are given in the following columns. B, V, and R magnitudes were obtained with VLT/FORS; i_{775} and z_{850} magnitudes are from *HST*/ACS; and the near-IR magnitudes are from the reprocessed VLT/ISAAC data. A value of 99 has been assigned to unavailable photometry. The last column gives the morphological T-type (de Vaucouleurs et al. 1976) of the galaxy, as determined by Postman et al. (2005).

The efficient selection criteria of targets based on high-quality imaging data has been a key piece in the success of our spectroscopic campaign. From a total number of 418 galaxies targeted with the 15 masks on FORS (see Table 1), we were able to obtain 282 (67%) redshifts, from which 227 (54%) correspond to secure measurements. We consider as cluster members all galaxies in the redshift range $1.22 < z < 1.25$, which corresponds to about $\pm 3\sigma_v$ around the cluster median velocity, where σ_v is the cluster velocity dispersion (see § 3.1). With this criterion, 38 galaxies are classified as spectroscopic cluster members (see Table 2). The signal-to-noise ratio (S/N) per resolution element of cluster member galaxies in the range 3995 Å $< \lambda < 4085$ Å rest-frame is observed to vary between ∼1 and ∼10. The redshifts and the corresponding error bars were obtained from the cross-correlation between the object and a template spectra as described in Demarco et al. (2005). In the cases of very poor S/N (∼ 1), the redshift was determined from the identification of [O II] ($\lambda 3727$) in the spectrum. In the case of passive galaxies, i.e., galaxies with an absorption-line spectrum and no visible emission lines, the redshift was obtained from the cross-correlation technique as

implemented in the RVSAO/XCSAO task in IRAF. In 23 objects (all with S/N > 2.5), Ca II (H+K) features were identified as well. However, further spectroscopic classification, such as the one proposed by Dressler et al. (1999) was not possible with the current data due to the lack of an accurate measurement of the Hδ ($\lambda 4102$) feature. In general, we avoided observing the same object more than once; however, we obtained more than one redshift measurement for a small number of objects. This allowed us to estimate total (random+systematic) errors, yielding typical values of $\delta z \sim 12 \times 10^{-4}$. This value represents a more rigorous estimate of the redshift errors, since the formal errors given by the cross-correlation (Tonry & Davis 1979) are known to be smaller than the true errors (e.g., Malumuth et al. 1992; Bardelli et al. 1994; Ellingson & Yee 1994; Quintana et al. 2000), and will be used in computations.

Those spectroscopic members for which FORS2 and ISAAC photometry is available (see Table 3) are shown in Figure 2. The red circles indicate spectroscopically confirmed non-emission-line members, while blue triangles indicate emission-line [O II] ($\lambda 3727$) confirmed members. The emission-line object in the

TABLE 4
X-Ray Point Sources, in the Cluster Field of View, Detected by *Chandra*

ID (1)	R.A. (2)	Decl. (3)	z (4)	$f_X[0.5-2]$ (5)	$f_X[2-10]$ (6)	$L_X[0.5-2]$ (7)	$L_X[2-10]$ (8)
425......................	12 52 58.14	−29 26 49.3	0.4694	5.1E−16	2.3E−15	3.3E+41	1.5E+42
69........................	12 53 03.60	−29 28 28.4	0.4762	1.1E−15	6.8E−15	7.3E+41	4.6E+42
7006....................	12 52 56.96	−29 30 10.9	0.7313	1.4E−15	3.3E−15	2.4E+42	5.7E+42
661......................	12 53 01.50	−29 25 38.8	0.7439	1.4E−14	2.6E−14	2.6E+43	4.8E+43
217......................	12 53 03.64	−29 27 42.1	0.7533	3.3E−16	9.0E−16	6.1E+41	1.7E+42
3043....................	12 53 00.39	−29 29 17.2	0.8220	2.9E−15	1.1E−14	6.5E+42	2.4E+43
355......................	12 52 42.48	−29 27 03.0	0.8440	4.2E−16	9.5E−16	9.9E+41	2.3E+42
612......................	12 52 59.93	−29 25 18.4	1.1764	1.1E−15	4.5E−15	5.5E+42	2.2E+43
174......................	12 52 49.82	−29 27 54.9	1.2382	1.9E−16	1.6E−15	1.1E+42	8.6E+42
321......................	12 52 40.36	−29 27 14.1	1.3479	1.6E−16	5.6E−15	1.1E+42	3.6E+43
374......................	12 52 50.08	−29 27 00.7	1.5198	1.6E−15	3.5E−15	1.4E+43	3.0E+43

Notes.—Cols. (2), (3): Units of right ascension are hours, minutes, and seconds, and units of declination are degrees, arcminutes, and arcseconds. Col. (4): Spectroscopic redshift of the source. Cols. (5), (6): Flux, in units of ergs s^{-1} cm-2, in the [0.5−2] and [2−10] keV bands of *Chandra*. Cols. (7), (8): Rest-frame X-ray luminosity, in units of ergs s^{-1}, in the [0.5−2] and [2−10] keV bands.

upper right side of the plot, marked with a square, corresponds to an X-ray source at the cluster redshift (ID 174; see Rosati et al. 2004; Martel et al. 2007). Note the unusual morphology of this source (see Fig. 5.3), with a faint red nucleus and an irregular, diffuse structure (also see Martel et al. 2007). In Table 4 we present the X-ray information corresponding to this source and other X-ray sources in the cluster FoV, for which a redshift measurement was obtained. The X-ray fluxes and rest frame X-ray luminosities in the soft ([0.5−2] keV) and hard ([2−10] keV) bands were extracted from the 190 ks *Chandra* observations (Rosati et al. 2004), assuming a power-law spectrum with photon index 1.4.

We estimated the success rate of our spectroscopic survey as the ratio of the number of objects with spectroscopic redshifts to the number of objects that were targeted for spectroscopy as a function of K_s (AB) magnitude. The data were binned in $\Delta K_s = 0.5$ mag intervals and include only objects for which an estimate of their K_s magnitude is available, as shown in Figure 3. Beside the overall success rate of our survey (*solid histogram*), the success rate for galaxies from the primary color-color selection (see § 2.1) is shown as the dashed histogram. A secondary color-color selection, defined by $I - z_{850} > 0.4$, $I - z_{850} < 0.85$, $V - I > 0.2$, $V - I < 1.2$, $V - I > [2.4 (I - z_{850}) - 1.12]$, and $V - I < [7.0 (I - z_{850}) - 2.3]$, was used to identify possible Balmer-break and star-forming galaxies. The success rate of this additional cut in color-color space is shown in Figure 3 as the dotted histogram. For galaxies within the primary color-color cut, the success rate decreases dramatically, from about 85% to about 20%, for galaxies with magnitudes fainter than 21.5 in K_s. At fainter magnitudes, the secondary color-color selection was more effective, as intended, at detecting sources with emission lines, increasing the number of galaxies per mask for which a redshift could easily be obtained. This secondary selection allowed us to obtain the redshift for 23 faint objects with $K_s > 21.5$. This corresponds to ~12% of all (no color restriction) targeted sources with $K_s > 21.5$. We note that all the sources within the $V - I$ versus $I - z_{850}$ cut with $K_s > 21.5$ and spectroscopic confirmation show some star-forming activity, while there are no targeted objects in this secondary color-color region with $K_s < 20.2$. The $V - I$ versus $I - z_{850}$ selection was intended to target star-forming galaxies at the cluster redshift; however, only eight members with [O II] were confirmed this way. In addition, no secure redshift was obtained for objects with $K_s < 20.5$ in this secondary color-color selecting area.

3. ANALYSIS

3.1. *Member Selection and Global Properties*

The distribution in redshift space of the 227 galaxies with a secure estimate of their redshift is shown in Figure 4. The bin size of the histogram is $\Delta z = 0.01$. We perform the adaptive-kernel method (hereafter DEDICA; Pisani 1993, 1996; Fadda et al. 1996; Girardi et al. 1996; Girardi & Mezzetti 2001) to search for the significant (>99% confidence level [c.l.]) peaks in the velocity distribution. This procedure detects RDCS J1252.9−2927
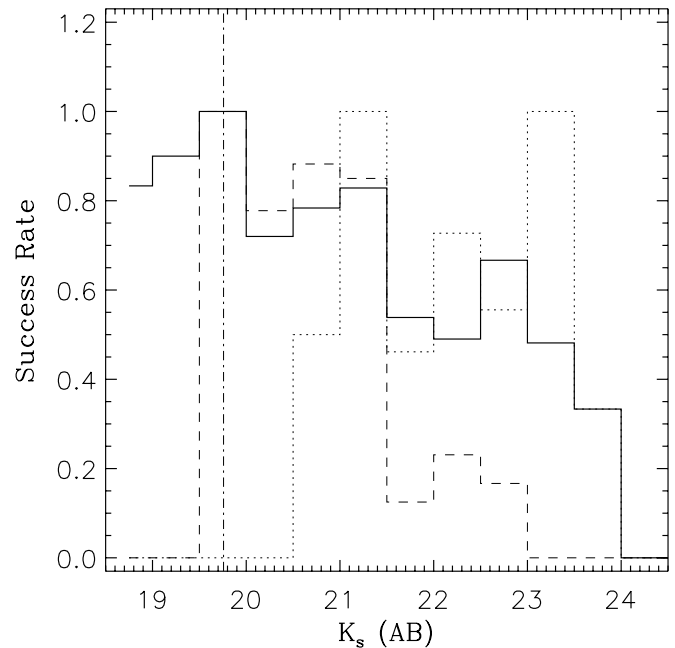

Fig. 3.—Success rate of the spectroscopic survey, defined as the ratio of the number of objects with spectroscopic redshifts to the number of objects that were targeted for spectroscopy as a function of K_s magnitude, shown by the solid histogram. The data were binned in $\Delta K_s = 0.5$ mag intervals. This distribution includes only objects for which an estimate of their K_s magnitude is available. The dashed histogram shows the success rate only considering our main color-color selection, $R - K_s > 3$ and $J - K_s < 2.1$, while the dotted histogram shows the same ratio only considering the secondary color-color selection: $I - z_{850} > 0.4$, $I - z_{850} < 0.85$, $V - I > 0.2$, $V - I < 1.2$, $V - I > [2.4(I - z_{850}) - 1.12]$, and $V - I < [7.0(I - z_{850}) - 2.3]$. This secondary selection was intended to target Balmer-break and star-forming galaxies. The dot-dashed line corresponds to the K_s magnitude of the brightest cluster member.
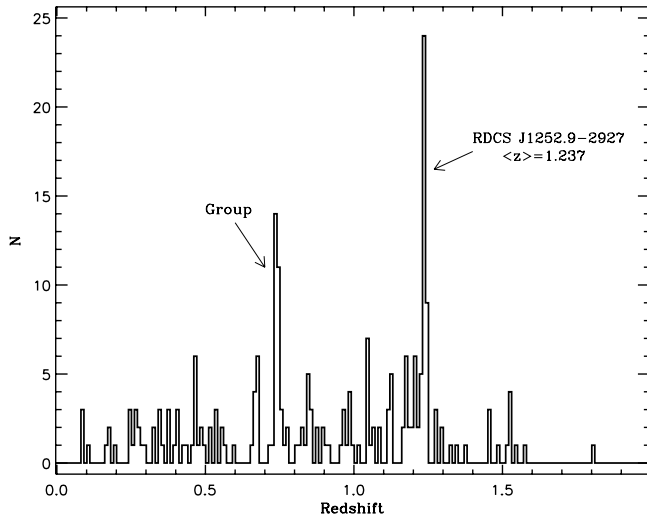
Fig. 4.—Redshift distribution of the 227 galaxies with a secure estimate of their redshifts. The bin size of the histogram is $\Delta z = 0.01$. RDCS J1252.9−2927 appears as the strongest peak of the distribution with a median redshift of $z = 1.2373$ (3 σ clipped mean of $\bar{z} = 1.2371 \pm 0.0009$), with 38 galaxies within the range $1.22 < z < 1.25$. A number of smaller peaks in the survey distribution are observed along the line of sight to the cluster, where a significant peak at $z \simeq 0.74$ is detected. This "group," composed of 31 galaxies, has a 3 σ clipped mean redshift of $\bar{z} = 0.7429 \pm 0.0024$.

as the strongest peak at $z \sim 1.24$ (see Fig. 4), populated by 38 galaxies (hereafter referred to as cluster members), the largest number of spectroscopic members discovered so far in a cluster of galaxies at $z > 1$, distributed over a region of 1.8 Mpc in radius. Out of non-member galaxies, 169 and 20 are foreground and background galaxies, respectively (see Table 5). In particular, 33 foreground galaxies belong to a dense peak at $z \sim 0.74$. This structure, in the redshift range $0.70 < z < 0.79$ (see Table 5), has a 3 σ clipped mean redshift of $\bar{z} = 0.7429 \pm 0.0024$. The projected distribution of these sources extends over a region of about $5.6'$ a side in front of the cluster, showing a small concentration of about 10 galaxies at about $1'$ north from the cluster center. There is no X-ray extended emission associated with this structure, indicating the lack of a hot gas component, although we note that there are three X-ray point sources at this redshift (see Table 4). This "group" may contribute to overestimations of the cluster mass obtained by weak-lensing analyses, as discussed in Lombardi et al. (2005).

By applying the biweight estimator to the cluster members (Beers et al. 1990), we compute a mean cluster redshift of $\langle z \rangle = 1.2370 \pm 0.0004$. We estimate the line-of-sight (LOS) velocity dispersion, σ_v, by using the biweight estimator and applying the cosmological correction and the standard correction for velocity errors (Danese et al. 1980). We obtain $\sigma_v = 747^{+74}_{-84}$ km s^{-1}, where errors are estimated through a bootstrap technique. The spectroscopic information available on the cluster member sample is given in Table 2, while the ACS and ground-based photometry of cluster members is presented in Table 3. Figure Set 5 show $5'' \times 5''$ thumbnail images of the 37 spectroscopic cluster galaxies in the FoV of ACS together with the corresponding FORS spectrum. The first two panels correspond to the i_{775} (rest-frame U) and z_{850} (rest-frame B) data. The most prominent spectral features identified in each spectrum in the displayed wavelength range are indicated (see figure caption for details). One cluster member, ID 7001, is out of the ACS FoV, and its spectrum is shown in Figure 6. For completeness, in Figure 7 we show the optical spectrum of the 10 non-cluster-member active galactic nuclei (AGNs) listed in Table 4. We do not present any analysis

TABLE 5
Spectroscopic Data of Field Galaxies

ID (1)	R.A. (2)	Decl. (3)	z (4)	z Error (5)
128........................	12 53 05.23	−29 28 08.2	0.0811	0.0008
723........................	12 52 44.53	−29 29 10.0	0.0844	0.0012
413........................	12 52 48.10	−29 26 50.7	0.0906	0.0011
29..........................	12 52 55.14	−29 28 49.5	0.1092	0.0009
787........................	12 52 49.99	−29 30 00.7	0.1637	0.0004
718........................	12 53 00.43	−29 24 35.3	0.1784	0.0010
624........................	12 52 59.72	−29 25 41.6	0.1798	0.0008
179........................	12 52 59.88	−29 27 50.4	0.1952	0.0007
502........................	12 52 40.33	−29 26 20.2	0.2461	0.0005
273........................	12 52 44.34	−29 27 29.6	0.2471	0.0001
219........................	12 52 44.27	−29 27 40.1	0.2476	0.0005
3096......................	12 52 45.39	−29 29 27.5	0.2604	0.0002
371........................	12 52 47.38	−29 27 02.5	0.2613	0.0008
31..........................	12 52 48.07	−29 28 42.2	0.2615	0.0007
535........................	12 52 51.52	−29 25 58.1	0.2693	0.0010
792........................	12 53 09.19	−29 27 36.3	0.2781	0.0006
746........................	12 53 05.03	−29 26 15.2	0.2788	0.0007
162........................	12 52 44.63	−29 28 00.3	0.2882	0.0007
594........................	12 52 48.67	−29 25 10.9	0.2979	0.0004
449........................	12 52 49.21	−29 26 39.1	0.3060	0.0001
72..........................	12 53 06.18	−29 28 28.6	0.3233	0.0005
241*......................	12 52 57.98	−29 27 36.2	0.3305	0.0005
250........................	12 52 46.42	−29 27 28.3	0.3452	0.0014
4052......................	12 53 06.44	−29 26 50.1	0.3483	0.0004
361........................	12 53 00.97	−29 27 04.0	0.3492	0.0001
341........................	12 52 54.73	−29 27 10.5	0.3515	0.0007
27..........................	12 52 50.15	−29 28 53.9	0.3749	0.0005
467........................	12 52 53.07	−29 26 31.4	0.3760	0.0006
325........................	12 52 40.53	−29 27 14.0	0.3962	0.0001
181........................	12 53 09.80	−29 27 51.6	0.4013	0.0004
180........................	12 52 56.32	−29 27 51.4	0.4050	0.0007
365........................	12 52 58.61	−29 27 03.0	0.4058	0.0004
790........................	12 52 59.31	−29 29 57.0	0.4296	0.0006
736........................	12 53 03.33	−29 24 17.1	0.4346	0.0006
730........................	12 52 44.87	−29 27 00.7	0.4602	0.0002
4010......................	12 53 10.59	−29 26 02.9	0.4687	0.0002
552........................	12 53 08.59	−29 25 58.4	0.4687	0.0006
629........................	12 52 56.07	−29 25 25.2	0.4689	0.0004
492........................	12 52 54.71	−29 26 23.1	0.4690	0.0004
269........................	12 52 56.13	−29 27 22.1	0.4692	0.0004
425........................	12 52 58.14	−29 26 49.3	0.4694	0.0006
69..........................	12 53 03.60	−29 28 28.4	0.4762	0.0005
22..........................	12 52 47.45	−29 28 56.7	0.4827	0.0004
714........................	12 53 09.89	−29 26 37.1	0.4861	0.0006
571........................	12 52 44.92	−29 25 47.2	0.4941	0.0007
153........................	12 52 47.06	−29 28 03.2	0.5110	0.0002
546........................	12 52 51.31	−29 25 58.1	0.5125	0.0009
656........................	12 52 48.90	−29 25 37.7	0.5375	0.0004
649........................	12 52 49.03	−29 25 37.4	0.5390	0.0004
469........................	12 52 45.78	−29 26 30.9	0.5408	0.0005
717........................	12 53 03.78	−29 24 34.9	0.5530	0.0005
788........................	12 52 52.25	−29 30 14.1	0.5573	0.0005
71..........................	12 53 08.30	−29 28 30.3	0.5616	0.0002
756........................	12 52 40.61	−29 27 10.3	0.5952	0.0006
377........................	12 53 00.10	−29 27 01.2	0.6678	0.0003
737........................	12 52 53.31	−29 24 43.3	0.6700	0.0005
127........................	12 52 59.38	−29 28 11.5	0.6701	0.0002
1............................	12 52 45.89	−29 29 04.0	0.6705	0.0005
222........................	12 52 53.09	−29 27 39.6	0.6719	0.0002
193........................	12 52 51.10	−29 27 49.0	0.6721	0.0002
528........................	12 52 57.67	−29 26 05.2	0.6723	0.0008
398........................	12 52 54.57	−29 26 48.5	0.6733	0.0003
405........................	12 53 00.24	−29 26 47.8	0.6744	0.0006
720........................	12 52 48.01	−29 29 10.0	0.6802	0.0006
441*......................	12 52 46.03	−29 26 40.1	0.7201	0.0004

TABLE 5—*Continued*

ID (1)	R.A. (2)	Decl. (3)	z (4)	z Error (5)
175*	12 52 58.98	−29 27 56.3	0.7217	0.0010
7006*	12 52 56.96	−29 30 10.9	0.7313	0.0002
508*	12 52 54.75	−29 26 14.7	0.7331	0.0003
537*	12 52 54.50	−29 26 05.4	0.7333	0.0003
465*	12 52 52.88	−29 26 31.9	0.7336	0.0003
495*	12 52 56.38	−29 26 22.3	0.7336	0.0002
488*	12 52 52.38	−29 26 23.3	0.7340	0.0002
458*	12 52 54.45	−29 26 31.6	0.7341	0.0003
539*	12 52 53.95	−29 26 05.6	0.7351	0.0003
713*	12 52 51.22	−29 30 21.2	0.7352	0.0003
231*	12 52 55.97	−29 27 35.9	0.7353	0.0004
519*	12 52 53.62	−29 26 10.1	0.7354	0.0001
225*	12 52 56.64	−29 27 39.9	0.7360	0.0002
6308*	12 52 48.75	−29 29 49.7	0.7364	0.0002
526*	12 52 56.74	−29 26 00.6	0.7394	0.0002
596*	12 53 01.65	−29 25 10.5	0.7397	0.0003
305*	12 52 50.43	−29 27 19.0	0.7424	0.0004
39*	12 52 58.52	−29 28 39.0	0.7425	0.0009
521*	12 53 08.70	−29 26 08.9	0.7431	0.0004
4043*	12 53 05.84	−29 26 42.2	0.7436	0.0002
3182*	12 52 53.17	−29 27 19.5	0.7437	0.0004
661*	12 53 01.50	−29 25 38.8	0.7439	0.0001
235*	12 53 08.72	−29 27 36.6	0.7447	0.0004
383*	12 53 08.67	−29 27 00.8	0.7458	0.0005
613*	12 52 56.00	−29 25 12.9	0.7470	0.0006
2060*	12 52 58.19	−29 25 36.2	0.7502	0.0001
217*	12 53 03.64	−29 27 42.1	0.7533	0.0003
411*	12 53 06.98	−29 26 50.5	0.7588	0.0003
511*	12 52 56.06	−29 26 15.1	0.7592	0.0004
4019*	12 53 12.36	−29 26 12.9	0.7635	0.0001
2007*	12 52 52.49	−29 29 25.0	0.7802	0.0003
551*	12 52 41.73	−29 25 56.2	0.7823	0.0007
380	12 52 49.65	−29 27 01.9	0.8208	0.0003
66	12 52 55.80	−29 28 32.2	0.8214	0.0003
3043	12 53 00.39	−29 29 17.2	0.8220	0.0001
402	12 52 49.53	−29 26 54.9	0.8226	0.0005
6309	12 52 44.95	−29 29 52.9	0.8348	0.0003
260	12 52 50.26	−29 27 27.5	0.8429	0.0004
208	12 52 50.97	−29 27 45.8	0.8434	0.0001
355	12 52 42.48	−29 27 03.0	0.8440	0.0002
408	12 52 50.75	−29 26 39.3	0.8462	0.0004
7003	12 52 43.44	−29 29 09.9	0.8474	0.0002
334	12 52 53.97	−29 27 08.4	0.8493	0.0003
389	12 52 57.19	−29 26 46.8	0.8523	0.0004
2456	12 53 01.62	−29 27 03.9	0.8531	0.0007
67	12 52 47.25	−29 28 29.2	0.8539	0.0004
503	12 52 52.85	−29 26 17.0	0.8750	0.0001
758	12 53 05.03	−29 27 37.1	0.8801	0.0003
199	12 52 46.53	−29 27 46.8	0.9002	0.0002
704	12 52 56.33	−29 25 00.5	0.9002	0.0004
755	12 52 41.88	−29 28 14.4	0.9026	0.0004
585	12 52 59.24	−29 25 46.5	0.9147	0.0002
701	12 52 42.61	−29 27 29.2	0.9551	0.0001
708	12 52 54.90	−29 29 26.7	0.9598	0.0015
536	12 52 56.75	−29 25 56.3	0.9662	0.0003
644	12 52 54.68	−29 25 29.6	0.9672	0.0002
500	12 52 56.77	−29 26 20.6	0.9677	0.0003
15	12 52 47.79	−29 28 57.9	0.9813	0.0002
566	12 53 07.21	−29 25 53.8	0.9815	0.0006
61	12 52 47.91	−29 28 33.7	0.9815	0.0003
60016	12 52 44.92	−29 30 28.1	0.9835	0.0002
734	12 52 40.07	−29 27 01.7	0.9881	0.0002
635	12 53 02.29	−29 25 41.7	0.9966	0.0004
3162	12 53 00.04	−29 26 28.5	1.0197	0.0001
95	12 52 53.35	−29 28 22.2	1.0436	0.0003
582	12 52 56.67	−29 25 43.5	1.0486	0.0005

TABLE 5—*Continued*

ID (1)	R.A. (2)	Decl. (3)	z (4)	z Error (5)
122	12 52 57.03	−29 28 14.3	1.0487	0.0003
715	12 53 09.21	−29 26 37.9	1.0488	0.0003
120	12 52 55.98	−29 28 12.4	1.0497	0.0002
615	12 52 57.05	−29 25 13.9	1.0497	0.0004
607	12 52 54.33	−29 25 10.3	1.0501	0.0003
2994	12 52 55.96	−29 29 08.4	1.0535	0.0002
643	12 52 49.11	−29 25 27.5	1.0690	0.0002
453	12 53 05.12	−29 26 29.4	1.0701	0.0004
3004	12 52 57.00	−29 29 09.8	1.0905	0.0003
707	12 52 59.26	−29 29 14.9	1.1149	0.0001
576	12 52 55.28	−29 25 49.3	1.1151	0.0005
648	12 53 03.18	−29 25 33.6	1.1205	0.0001
617	12 53 01.32	−29 25 17.8	1.1214	0.0002
523	12 52 57.86	−29 26 08.5	1.1215	0.0002
658	12 53 03.16	−29 25 39.1	1.1221	0.0002
652	12 53 03.34	−29 25 37.7	1.1222	0.0002
336	12 52 43.73	−29 27 09.5	1.1224	0.0005
653	12 52 52.45	−29 25 36.1	1.1228	0.0002
2806	12 52 45.46	−29 28 23.9	1.1682	0.0003
2983	12 52 50.45	−29 29 09.1	1.1706	0.0002
6302	12 53 05.91	−29 25 10.8	1.1733	0.0002
610	12 52 58.60	−29 25 15.1	1.1747	0.0004
634	12 52 58.13	−29 25 41.2	1.1755	0.0003
612	12 52 59.93	−29 25 18.4	1.1764	0.0003
24	12 52 53.43	−29 28 51.7	1.1772	0.0004
456	12 53 03.00	−29 26 35.8	1.1775	0.0003
646	12 52 58.33	−29 25 33.0	1.1813	0.0003
448	12 52 58.79	−29 26 37.0	1.1871	0.0002
2993	12 52 53.19	−29 29 08.8	1.1939	0.0002
93	12 52 45.62	−29 28 21.5	1.1940	0.0002
2545b	12 53 02.07	−29 27 20.8	1.2055	0.0003
25	12 52 58.07	−29 28 52.3	1.2087	0.0003
4001	12 53 08.39	−29 25 50.2	1.2092	0.0002
308	12 53 02.12	−29 27 19.4	1.2095	0.0002
44	12 52 57.89	−29 28 44.2	1.2103	0.0003
2545	12 53 02.06	−29 27 21.7	1.2105	0.0003
574	12 52 59.86	−29 25 46.9	1.2119	0.0002
581	12 52 58.74	−29 25 47.5	1.2148	0.0002
716	12 52 40.38	−29 27 45.6	1.2714	0.0003
392	12 53 05.05	−29 26 58.8	1.2720	0.0003
311	12 52 53.76	−29 27 16.1	1.2751	0.0002
2824	12 52 53.53	−29 28 28.6	1.2940	0.0002
3018	12 52 50.13	−29 29 16.8	1.2949	0.0003
147	12 52 52.48	−29 28 03.4	1.3259	0.0007
420	12 52 41.19	−29 26 50.9	1.3470	0.0005
321	12 52 40.36	−29 27 14.1	1.3479	0.0009
357	12 53 03.00	−29 26 58.9	1.3725	0.0003
33	12 52 47.91	−29 28 50.2	1.4566	0.0003
60005	12 52 46.80	−29 29 44.6	1.4586	0.0006
10	12 52 52.50	−29 29 00.7	1.4652	0.0003
2585	12 52 53.62	−29 27 28.5	1.4847	0.0003
374	12 52 50.08	−29 27 00.7	1.5198	0.0003
50	12 52 44.92	−29 28 43.1	1.5219	0.0004
2710	12 52 49.20	−29 28 03.3	1.5235	0.0004
401	12 52 56.67	−29 26 55.8	1.5245	0.0002
197	12 52 49.94	−29 27 50.4	1.5254	0.0005
2987	12 52 47.85	−29 29 21.1	1.5765	0.0003
60013	12 53 02.39	−29 24 52.4	1.8065	0.0008

NOTES.—Col. (1): Object ID in the catalog. Cols. (2), (3): Right ascension (R.A.) and declination (Decl.), J2000 coordinates. Units of right ascension are hours, minutes, and seconds, and units of declination are degrees, arcminutes, and arcseconds. Cols. (4), (5): Redshift and formal error in redshift as obtained from the cross-correlation. The table has been ordered from low to high redshift. A prominent ''structure'' in redshift can be seen at redshift $z \sim 0.74$ (see § 3.1). Objects belonging to this ''structure'' are marked with an asterisk.
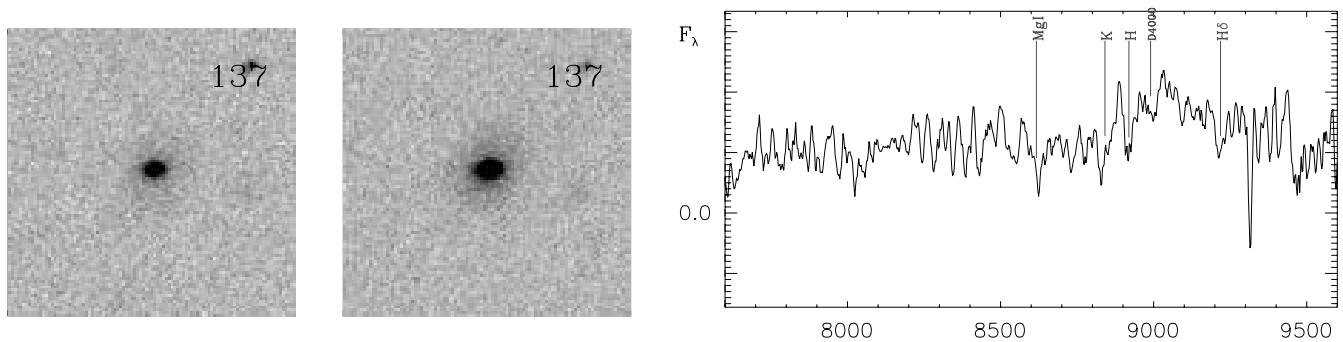
Fɪɢ. 5.1. Galaxy 137

Fɪɢ. Sᴇᴛ 5.—The sample of 37 spectroscopic members in the ACS field of view. The left and middle panels show ACS cutouts in the i_{775} and z_{850} bands, respectively. Each cutout is 5″ a side, and the number in the panels corresponds to the galaxy ID. The right panel shows the corresponding VLT/FORS spectrum. The most prominent spectral features identified in each spectrum in the wavelength range shown here are marked (see footnote in Table 2 for the list of spectral features). The spectra have been smoothed by 5 pixels (1 pixel $\sim$ 2.5 Å). [*See the electronic edition of the Journal for Figs. 5.2–5.37*]

of the spectroscopic properties of these sources, as this is beyond the scope of this work. Figure 8 shows the distribution of RDCS J1252.9−2927 member galaxies in velocity and redshift space. The hatched area indicates the distribution of star-forming members. The secondary selection in $V - I$ versus $I - z_{850}$ allowed the discovery of 8 of the 17 cluster members with [O ɪɪ] ($\lambda3727$) emission lines. If we separate cluster members into two categories, passive and star-forming galaxies, there is no significant offset in median velocity between the two categories (see Fig. 8). The mean redshift of passive and emission-line [O ɪɪ] spectroscopic members is 1.2373 ± 0.0057 and 1.2369 ± 0.0054, respectively. The velocity dispersions of these populations are also consistent with each other and with the overall cluster velocity dispersion, within the uncertainties.

In Figure 9 we show the rest-frame velocity versus projected distance from the cluster center (*bottom panel*). Hereafter we consider as cluster center the position of the X-ray center (Rosati et al. 2004): R.A. $12^h52^m54.4^s$, decl. $-29°27'17.5''$ (J2000.0). We also show the rest-frame velocities of the three brightest cluster members (IDs 291, 247, and 289, hereafter referred to as BCM1, BCM2, and BCM3). BCM1 is about 0.3 mag brighter in K_s than BCM2 and BCM3 (Fig. 9, *top panel*). BCM1 and BCM3 are closely located near the position of the X-ray center and the peak of the galaxy distribution as recovered from the two-dimensional DEDICA method.

Assuming that RDCS J1252.9−2927 is in dynamical equilibrium (this will be discussed in § 4), we can compute global virial
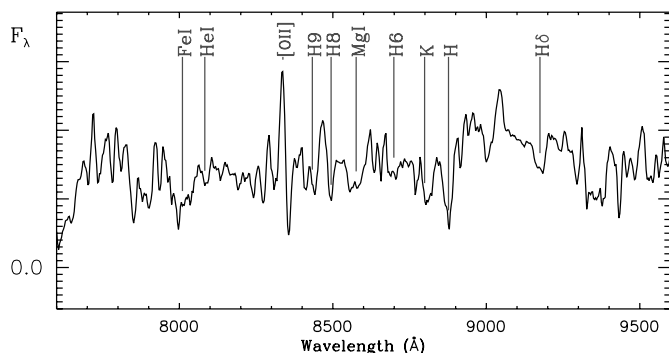

Fɪɢ. 6.—VLT/FORS spectrum of cluster member ID 7001. This object was discovered outside the ACS field of view. Most prominent spectral features in the wavelength range shown here are marked (see footnote in Table 2 for the list of spectral features). The spectrum has been smoothed by 5 pixels (1 pixel $\sim$ 3.1 Å). [*See the electronic edition of the Journal for a color version of this figure.*]

quantities. Following the prescriptions of Girardi & Mezzetti (2001), we assume for the radius of the quasi-virialized region $R_{\mathrm{vir}} = R_{178} = 0.17 \times \sigma_v/H(z) = 1.61$ Mpc (see their eq. [1] after introducing the scaling with $H(z)$; see also eq. [8] of Carlberg et al. [1997] for R_{200}). Therefore, our spectroscopic catalog samples the whole cluster virialized region. We can compute the mass using the virial theorem (Limber & Mathews 1960; Girardi et al. 1998) under the assumption that the galaxies trace the total mass,

$$M = M_{\mathrm{svir}} - \mathrm{SPT}, \qquad (3)$$

where

$$M_{\mathrm{svir}} = \left(\frac{3\pi}{2}\right)\left(\frac{\sigma_v^2 R_{\mathrm{PV}}}{G}\right) \qquad (4)$$

is the standard virial mass, R_{PV} a projected radius (equal to 2 times the harmonic radius), and SPT is the surface pressure term correction (The & White 1986). The estimate of σ_v is generally robust when computed within a large cluster region, as shown in Figure 10. At radii larger than 1.4 Mpc, the profile becomes flatter, consistent with observations of low-redshift clusters (Girardi et al. 1996; Fadda et al. 1996), suggesting that at large cluster radii any velocity anisotropy of cluster galaxies does not affect the value of $\sigma_v(<R)$. We thus consider the above global value, σ_v, as the cluster velocity dispersion. The value of R_{PV} depends on the size of the considered region, so that the computed mass increases (but not linearly) when increasing the considered region. Using the 37 galaxies within R_{vir}, we obtain $R_{\mathrm{PV}} = 1.09 \pm 0.15$ Mpc. As for the SPT correction, we assume a correction factor of 20%, which we obtained by combining data on many clusters (e.g., Carlberg et al. 1997; Girardi et al. 1998). This leads to a virial mass $M(<R_{\mathrm{vir}} = 1.61$ Mpc$) = 5.3^{+1.3}_{-1.4} \times 10^{14}$ $M_\odot$.

We also used an alternative estimate of the virial mass (see eq. [13] of Girardi et al. 1998). This alternative estimate is based on the knowledge of the galaxy distribution and, in particular, a galaxy King-like distribution with parameters typical of nearby/medium-redshift clusters: a core radius $R_{\mathrm{core}} = 1/20 \times R_{\mathrm{vir}}$ and a slope parameter $\beta_{\mathrm{fit}} = 0.8$ (which gives a volume galaxy density at large radii as $r^{-3\beta_{\mathrm{fit}}} = r^{-2.4}$; Girardi & Mezzetti 2001). For the whole virialized region we obtain $R_{\mathrm{PV}} = 1.20$ Mpc, where a 25% error is expected due to the fact that typical, rather than individual, galaxy distribution parameters are assumed. This leads to a virial mass $M(<R_{\mathrm{vir}} = 1.61$ Mpc$) = 5.9^{+1.9}_{-2.0} \times 10^{14}$ $M_\odot$, in good agreement with the above value.
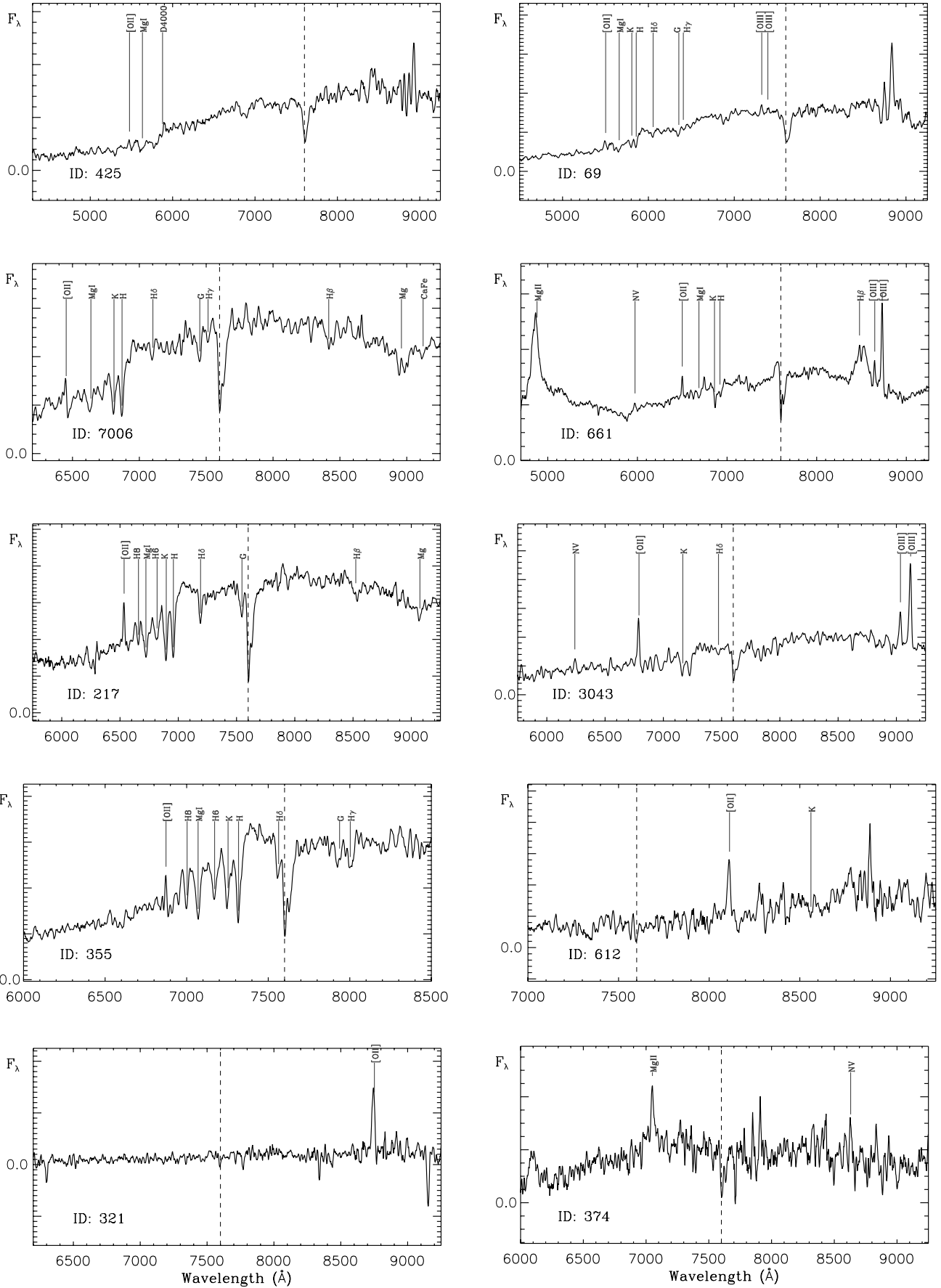
FIG. 7.—Optical spectrum of a spectroscopically identified non-cluster-member AGNs in the field of view of RDCS J1252.9−2927. Most prominent spectral features are indicated: Mg I (λ2798), N v, [O II] (λ3727), H8, Mg I (λ3834), H6, Ca II (H), Ca II (K), D4000, Hδ, G, Hγ, Hβ, [O III], Mg, and CaFe. The vertical dashed line indicates the telluric *A*-band feature at 7600 Å. The spectra have been smoothed by 5 pixels (1 pixel ∼ 3.0 Å). [*See the electronic edition of the Journal for a color version of this figure.*]
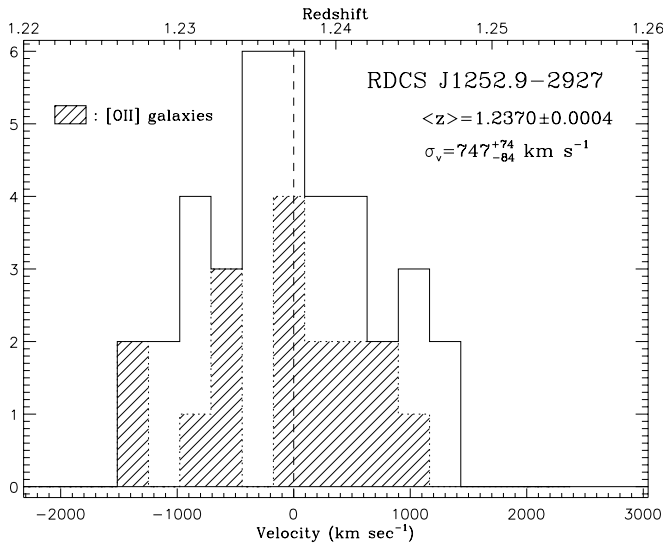
Fig. 8.—Redshift and velocity distribution of cluster members. The y-axis indicates the number of objects, and the histogram bin size has been set to $\Delta z = 0.002$. Assuming a Gaussian distribution in velocity of the spectroscopic members, the median redshift of the distribution is $z = 1.2373$ (*vertical dashed line*), and the global velocity dispersion is 747^{+74}_{-84} km s^{-1}, based on the biweight estimator (Beers et al. 1990). The hatched area indicates the distribution of star-forming ([O II] ($\lambda 3727$)) members. The mean redshift and velocity dispersion of passive and [O II] cluster members are consistent with each other and with the overall cluster values within the uncertainties.

To compare our result with the estimate obtained from the X-ray data for a smaller cluster region (Rosati et al. 2004), we assume that the cluster is described by a King-like mass distribution (see above) or, alternatively, a NFW profile where the mass-dependent concentration parameter is taken from Navarro et al.
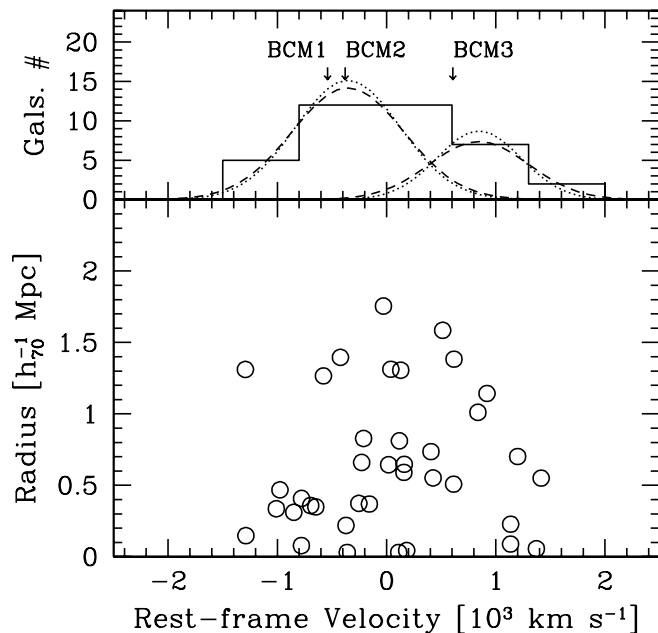
Fig. 9.—*Bottom*: Rest-frame velocity vs. projected distance from the cluster center (taken as the X-ray center; Rosati et al. 2004) of the 38 galaxies assigned to the cluster. *Top*: Velocity histogram of the 38 galaxies assigned to the cluster (*solid line*). Velocities of the three brightest galaxies are pointed out. The two dashed Gaussians correspond to the 3D KMM partition (KMM1 and KMM2, from left to right) while the dotted Gaussians indicate the two groups detected by the WGAP procedure (WGAP1 and WGAP2, from left to right). The 3D diagnostics is, in general, the most sensitive indicator of the presence of substructure. Therefore, we consider the KMM groups as a robust characterization of the cluster substructure.
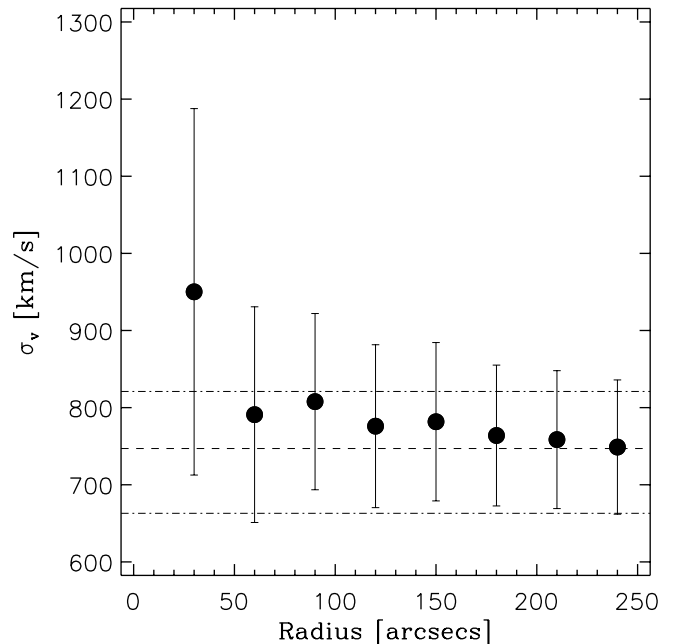
Fig. 10.—Rest-frame integrated velocity dispersion profile of RDCS J1252.9−2927. At the cluster redshift ($z = 1.237$), 0.5′ corresponds to 250 kpc. The dashed line indicates the overall rest-frame cluster velocity dispersion ($\sigma_v = 747^{+74}_{-84}$ km s^{-1}) obtained from the biweight estimator (Beers et al. 1990), with the corresponding error bars as dot-dashed lines. The filled circles are the integrated rest-frame velocity dispersion calculated at the given radius by using all the galaxies within that radius (Girardi et al. 1996). These values were obtained by using Tukey's biweight estimator (Press et al. 1992), correcting for velocity errors (Danese et al. 1980). Error bars are obtained from the fractional uncertainty in estimate for σ_v (Taylor 1997). The cluster velocity dispersion values are observed to be robust at radii larger than 170″ (1.4 Mpc), i.e., at these radii, any velocity anisotropy of cluster galaxies does not affect the value of $\sigma_v(<R)$.

(1997) and rescaled by the factor $1 + z$ (Bullock et al. 2001; Dolag et al. 2004). We obtain $M_{\mathrm{proj}}(<R = 0.536 \text{ Mpc}) = (1.6 - 2.3) \times 10^{14} \, M_\odot$, in good agreement with that found by Rosati et al. (2004). This value is also in agreement with that found by Ettori et al. (2004) within a similar projected radius. Using the same mass distributions we also compute the projected mass within 1 Mpc for comparison with the weak-lensing analysis by Lombardi et al. (2005). The cluster mass distribution is truncated at one virial radius or, alternatively, at two virial radii. The range of our results is $M_{\mathrm{proj}}(<R = 1 \text{ Mpc}) = (4.5-6.3) \times 10^{14} \, M_\odot$, in agreement with Lombardi et al. (2005), when taking into account the uncertainties on the mass values, although systematically lower.

By comparing the cluster X-ray luminosity (Rosati et al. 2004) and the cluster velocity dispersion derived above with the L_X-σ_v relation presented in Figure 2 of Xue & Wu (2000), we see a good agreement between the observed L_X and σ_v values in RDCS J1252.9−2927 and those from >100 galaxy clusters selected from the literature. Using the best-fit σ_v-T relation from Xue & Wu (2000) without taking into account the fit errors, we obtain a temperature of $T = 3.89^{+0.61}_{-0.65}$ keV for a velocity dispersion of $\sigma_v = 747^{+74}_{-84}$ km s^{-1}. This temperature is more than 3 σ away from the observed value of $T_X = 6.0^{+0.7}_{-0.5}$ keV (Rosati et al. 2004), and still ~0.5 σ lower if the fit errors are considered.

3.2. Substructures and Projected Distribution

We analyze the velocity distribution to look for possible deviations from Gaussianity that could provide important signatures of complex dynamics. For the following tests the null hypothesis is that the velocity distribution is a single Gaussian.
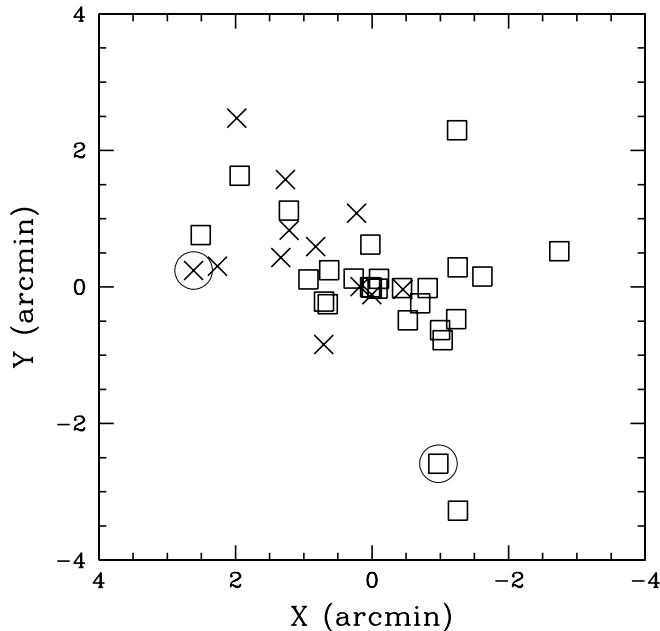
Fig. 11.—Projected distribution on the sky of the 38 member galaxies: open squares and crosses indicate galaxies assigned to KMM1 and KMM2 groups, respectively. The two large open circles indicate the two galaxies that give the difference in membership with WGAP1 and WGAP2 groups. The plot is centered on the X−ray cluster center. KMM1 is mostly located to the west of the cluster center, while KMM2 is mostly to the east, and the degree of merging observed from galaxy positions shows that these two groups have already started virialization in the main cluster potential.

We compute three shape estimators, i.e., the kurtosis, the skewness, and the scaled tail index (see, e.g., Beers et al. 1991). The value of the normalized kurtosis (−0.754) shows evidence that the velocity distribution differs from a Gaussian, being lighter tailed, with a c.l. of ∼95%−99% (see Table 2 of Bird & Beers 1993).

Then we investigate the presence of gaps in the distribution. A weighted gap in the space of the ordered velocities is defined as the difference between two contiguous velocities, weighted by the location of these velocities with respect to the middle of the data. We obtain values for these gaps relative to their average size, precisely the mid-mean of the weighted-gap distribution. We look for normalized gaps larger than 2.25, since in random draws of a Gaussian distribution they arise in at most about 3% of the cases, independent of the sample size (Wainer & Schacht 1978; Beers et al. 1991). One significant gap in the ordered velocity data set is detected dividing the data set into two subsets containing 26 and 12 galaxies from "low" to "high" velocities (hereafter referred to as the WGAP1 and WGAP2 groups; see top panel in Fig. 9). We compare these two subsets applying the two-dimensional Kolmogorov-Smirnov tests to the galaxy positions (2DKS test; see Fasano & Franceschini 1987), as implemented by Press et al. (1992). In spite of the modest statistics, we find a marginal significance (89% c.l.) for the difference. The "high" velocity WGAP2 group is located to the east of the "low" velocity group WGAP1 (see Fig. 11).

To further investigate the substructure membership we use the Kaye's mixture model (KMM) test as implemented by Ashman et al. (1994). The KMM algorithm fits a user-specified number of Gaussian distributions to a data set and assesses the improvement of that fit over a single Gaussian. In addition, it provides the maximum likelihood estimate of the unknown n-mode Gaussians and an assignment of objects into groups. However, one of the major uncertainties of this method is the optimal choice of the

number of groups for the partition. Using the results of the gap analysis, we decide to fit two groups and determine the first guess for the group partition. We do not find any group partition which provides a significantly better description of the velocity distribution with respect to a single Gaussian in the one-dimensional (1D) analysis. However, since the three-dimensional (3D) diagnostic is, in general, the most sensitive indicator of the presence of substructure (e.g., Pinkney et al. 1996), we apply the 3D version of the KMM software using simultaneous galaxy velocity and position. In the 3D case we find that a two-group partition of 26 and 12 galaxies (hereafter the KMM1 and KMM2 groups) better describes the velocity distribution at the 95.6% c.l., according to the likelihood ratio test (see Fig. 9). These groups are located at -354 ± 159 and 845 ± 182 km s^{-1} with respect to the cluster mean velocity, and to the west and east of the cluster center, respectively. The velocity dispersions of KMM1 and KMM2 are estimated to be 486^{+47}_{-85} and 426^{+57}_{-105} km s^{-1}, respectively. This partition corresponds to that indicated by the weighted gap analysis with the difference of two galaxies (see Fig. 11). These velocity dispersion values are less robust than the overall cluster velocity dispersion due to uncertainties in the membership of galaxies in KMM1 and KMM2, although the detection and location of the substructures are reliable. By assuming dynamical equilibrium and theoretically estimating R_{PV} for each KMM group, as done in § 3.1 for the whole cluster, we obtain masses of $M(<R_{200} = 1.05 \text{ Mpc}) = 1.6^{+0.5}_{-0.7} \times 10^{14}$ $M_{\odot}$ for KMM1 and $M(<R_{200} = 0.92 \text{ Mpc}) = 1.1^{+0.4}_{-0.6} \times 10^{14}$ $M_{\odot}$ for KMM2. We note that the sum of these masses is about the half of the cluster mass; we will come back to this in § 4.

To look for further evidence that RDCS J1252.9−2927 is still not completely dynamically relaxed, we analyzed the velocity of the brightest galaxy BCM1. In fact, since its location coincides with the X−ray center, it is expected that BCM1 is at the center of the cluster potential and thus at the center of the velocity distribution. We find that BCM1 shows evidence of peculiarity at the >95% c.l. according to the Indicator test by Gebhardt & Beers (1991), while it lies very close to the peak of the velocity distributions of KMM1 (see Fig. 9). We finally note that the close pair of luminous galaxies BCM1 and BCM3 are separated by ∼550 km s^{-1} in rest-frame velocity and, as first noted by Blakeslee et al. (2003b), in interaction, as supported by Rettura et al. (2006), who see signs of interaction in the form of an S-shaped residual after galaxy subtraction linking the two galaxy centers. In addition, BCM2 is near the edge of the coma-like structure of the X-ray surface brightness reported by Rosati et al. (2004).

In Figure 1 we show the projected distribution of RDCS J1252.9−2927 spectroscopic members on the plane of the sky.[21] Circles are passive galaxies, and triangles are emission line members. The overall shape of the distribution of confirmed galaxy members is clearly elongated in the east-west direction, as previously reported in Toft et al. (2004) based on the K_s-band light distribution of photometric cluster members, although more uniform than that of other high-redshift clusters (see, e.g., Gioia et al. 1999; Demarco et al. 2005; Girardi et al. 2005). The projected distribution of the KMM groups is consistent with the overall cluster galaxy distribution, suggesting that the observed elongation is caused by the merger of both groups.

3.3. Spectral Properties of Cluster Galaxies

The spectral features of cluster members indicate the stellar content of galaxies in RDCS J1252.9−2927, and the [O II] line

---

[21] The background image corresponds to the ACS combined i_{775}- and z_{850}-band data.

was used to estimate the SFR for some members. The spectrum of each of the 37 cluster members in the ACS FoV is shown in the last panel for each object in Figure Set 5, while the spectrum of the spectroscopic member outside the FoV of ACS is shown in Figure 6. The flux calibration of the spectra is not accurate in the very red. Following Homeier et al. (2005) we estimated the SFR for the 17 member galaxies with [O II] $\lambda3727$ in their spectra. We measured the integrated flux of the [O II] line using the bandpass defined in Tran et al. (2003). In two cases with a very low S/N continuum (IDs 174 and 9000), the [O II] line flux was underestimated due to sky oversubtraction. Previous to these measurements, all the spectra were Doppler corrected by using the task `dopcor` in IRAF. These line fluxes were converted into $L_{[O\,II]}$ luminosities by assuming that all these galaxies are at the same distance, corresponding to the median redshift of the cluster ($z = 1.237$). SFRs were derived from the $L_{[O\,II]}$ values by following the prescription of Kewley et al. (2004):

$$\mathrm{SFR}_{[O\,II]}(M_\odot\ \mathrm{yr}^{-1}) = (6.58 \pm 1.65) \times 10^{-42} L_{[O\,II]}(\mathrm{ergs\ s}^{-1}),$$

(5)

which takes into account the mean reddening-corrected [O II]/Hα = (1.2 ± 0.3) ratio from the Nearby Field Galaxies Survey (Jansen et al. 2000). We do not correct for metallicity or dust extinction effects on the [O II] flux measurements, so our SFRs estimates should be considered as lower limits to the true SFR. The [O II] line can be considerably affected by dust absorption, giving SFRs 1 or 2 orders of magnitude lower than SFRs unaffected by dust at 15 μm (Duc et al. 2002; Coia et al. 2005). A more robust SFR indicator is the Hα line (see, e.g., Charlot & Longhetti 2001); however, at the cluster redshift this line is not observed in the optical. IR luminosities can also be used as reasonable tracers of SFR in galaxies (Kewley et al. 2002; Calzetti et al. 2005). Integrated [O II] line flux measurements, [O II] equivalent widths, and SFR values derived from $L_{[O\,II]}$ of star-forming cluster galaxies are given in Table 2. Error bars are estimated by taking into account the rms fluctuation in flux within the two sidebands at both sides of the [O II] bandpass, as defined in Tran et al. (2003). The median value of the derived SFRs is 0.7 $M_\odot$ yr^{-1}, with a few galaxies reaching SFRs greater than 2.0 $M_\odot$ yr^{-1} (see Table 2). Typical errors in the SFR are about 47%, reaching values greater than 60% in a couple of cases. Our median SFR value is consistent within the errors with the mean SFR ($0.17 \pm 0.02\ h_{100}^{-2}\ M_\odot$ yr^{-1}) derived by Balogh et al. (1998) from the [O II] ($\lambda3727$) emission line for cluster galaxies at large ($R_{200} \sim 1.5-2\ h_{100}^{-1}$ Mpc) clustercentric radii and in the redshift range $0.18 < z < 0.55$. These values are, however, much lower than that of $\sim3\ h_{100}^{-2}\ M_\odot$ yr^{-1} derived for cluster galaxies at $z \sim 0.75$ from Hα (Finn et al. 2005), and even lower than the Hα SFR of field galaxies at $z \sim 1$ (Glazebrook et al. 1999; Doherty et al. 2004). In spite of the little or no evolution in SFR between the sample of Balogh et al. (1998) and our sample, this comparison can be affected by dust (see § 3.5) and metallicity effects on the [O II] line; therefore, a fair comparison requires Hα and IR measurements of the true SFR in order to quantify the amount of evolution. The lack of SFR measurements in cluster galaxies at $z > 1$ and the limitations of our data prevent us from studying the evolution of the SFR in clusters from $z \sim 1.3$ down to the local universe.

The co-added spectrum of the 17 star-forming cluster members is shown in Figure 12. The presence of young stellar populations (A- and F-type stars) is inferred by the detection of Balmer absorption lines. Most of these galaxies present irregular,
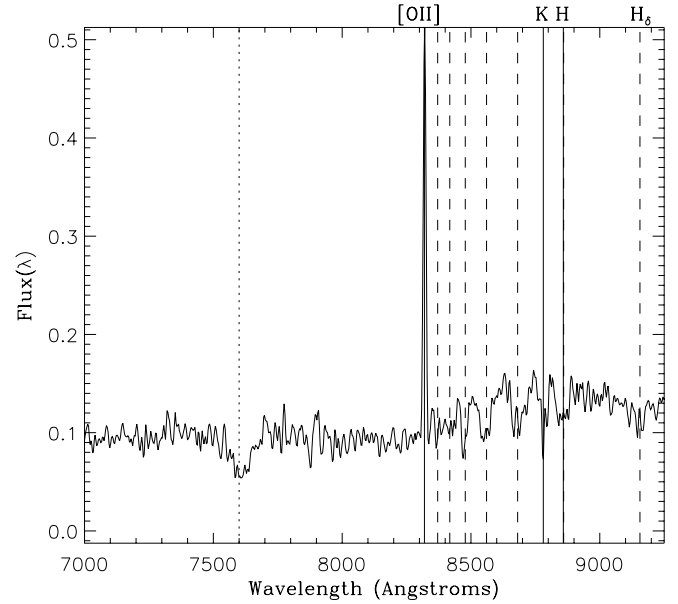

Fig. 12.—Co-added spectrum of the 17 spectroscopically confirmed star-forming members in RDCS J1252.9−2927. The most prominent spectral features in the displayed wavelength range are indicated. From right to left, the dashed lines are features of the Balmer series: Hδ, Hϵ (next to the Ca II H line), and the higher order features H6, H7, H8, H9, and H10. The solid lines are the [O II] ($\lambda3727$) emission feature and the Ca II K and H absorption features. The dotted line indicates the A-band telluric feature at 7600 Å. The spectrum has been smoothed by 5 pixels (1 pixel $\sim$ 3.1 Å).

extended features, most likely the home for the young stars and where most of the star-forming activity takes place. In particular, we note that object ID 6306, with an $i_{775} - z_{850} = 0.85$ color, presents a spectrum showing a young poststarburst component (prominent Balmer absorption features) in addition to ongoing star formation activity ([O II] in emission; see Fig. 5.35). This galaxy can therefore be classified as an E+A+[O II] galaxy (e.g., Demarco et al. 2005). We also note that ID 7001 has similar characteristics.

On the other hand, there is an indication of the remaining traces of the latest episode of star formation in some of the massive, passive early-type galaxies in the cluster. Due to the lower S/N of our spectra at wavelengths larger than about 9000 Å, an accurate measurement of the EW of the Hδ absorption feature is not possible. Therefore, an identification of the poststarburst stellar populations in individual early-type cluster galaxies cannot be properly done with the existing data. However, by co-adding the spectra of the 10 brightest passive galaxies in RDCS J1252.9−2927 (Rosati 2004), a prominent Hδ feature emerges and some other higher order Balmer features become visible. In Figure 13 we show the co-added spectra of the 10 (*top panel*) and 20 (*bottom panel*) brightest (in K_s) passive cluster members. An increase of the Hδ (about 36%) and other Balmer absorption features equivalent width can be seen when including fainter early-type members. We note that the Hδ absorption line can indeed clearly be seen in the individual spectrum of the first, second, third, and fifth brightest cluster members (in z_{850}) after a total integration time of 24 hr (Holden et al. 2005). A more detailed quantitative analysis of this observation is underway (P. Rosati et al., in preparation).

3.4. Color-Magnitude Distribution of Cluster Galaxies

Lidman et al. (2004) included all galaxies within 20″ (0.17 Mpc) of the cluster center in their $J - K_s$ versus K_s color-magnitude
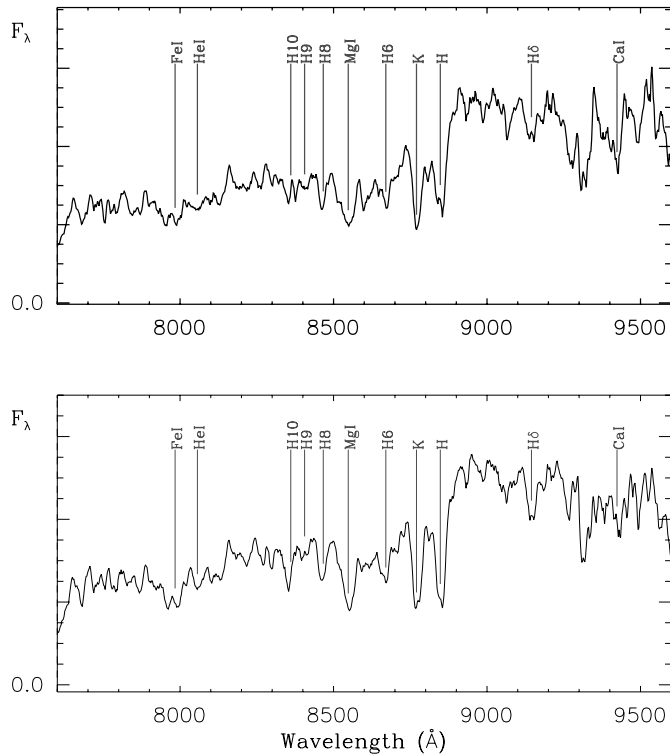
FIG. 13.—Co-added spectrum of the 10 (*top*) and 20 (*bottom*) brightest (in K_s) passive cluster members. Prominent Balmer absorption features become visible by co-adding spectra, indicating the existence of poststarburst stellar populations in passive early-type galaxies at this redshift (see footnote in Table 2 for a list of spectral features). The spectra have been smoothed by 5 pixels (1 pixel ∼ 2.5 Å). [*See the electronic edition of the Journal for a color version of this figure.*]
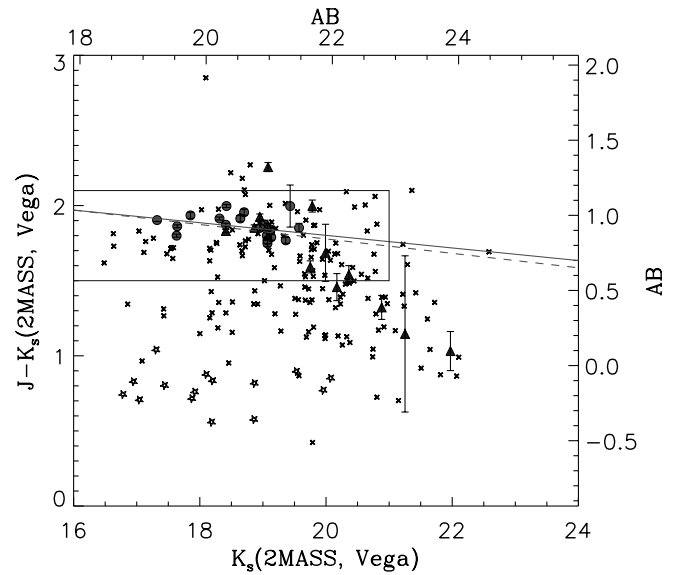

FIG. 14.—Near-IR (reprocessed ISAAC data) color-magnitude diagram (CMD) of spectroscopic cluster members. Colors and magnitudes are shown in the 2MASS (Carpenter 2001; Cohen et al. 2003) and AB systems. The star symbols represent spectroscopically confirmed stars. Crosses are non-cluster members, i.e., objects with redshift $z \leq 1.22$ or $z \geq 1.25$. Filled red circles are spectroscopic cluster members (objects with redshift in the range $1.22 < z < 1.25$) without detectable [O II] ($\lambda 3727$) emission. The filled blue triangles are cluster members with [O II] emission. The dotted red line is the fit published in Lidman et al. (2004), including only galaxies within 20″ (0.17 Mpc) of the cluster center and within the blue rectangle. The solid red line (fit 2 in Table 6) is the fit presented in this work using only cluster members without [O II] (*filled red circles*). The slope and scatter about the two fits are listed in Table 6. The reddest star-forming member in the diagram corresponds to the confirmed AGN (ID 174). In this study we extend the analysis of the color-magnitude diagram of RDCS J1252.9−2927 to more than 1 Mpc in radius from the cluster center, and show that the red sequence extends to more than 0.5 Mpc in clustercentric radius. [*See the electronic edition of the Journal for a color version of this figure.*]

diagram of RDCS J1252.9−2927. In this paper, we produce a second color-magnitude diagram using the reprocessed ISAAC data, but here we only use galaxies with measured redshifts. The stellar symbols in Figure 14 represent spectroscopically confirmed stars. Crosses are non-cluster members, i.e., objects with redshift $z \leq 1.22$ or $z \geq 1.25$. Filled circles are cluster members without detectable [O II] ($\lambda 3727$) emission. The filled triangles, on the other hand, are cluster members with [O II] emission. The dotted red line is the fit published in Lidman et al. (2004). At that time, only a limited number of redshifts were available, so, to limit the effect of contamination from non-cluster members, only galaxies within 20″ of the cluster center and within the blue rectangle in Figure 14 were used in fitting the CM relation. Here, only cluster members without [O II] are used in the fit, which is shown as the solid red line. No other restrictions are used. The slope and scatter about the two fits are listed in Table 6 and are calculated as explained in Lidman et al. (2004). Within the statistical error both fits are the same. Therefore, as in Lidman et al. (2004), the values obtained here for the slope and scatter about the new fit imply that passive galaxies in RDCS J1252.9−2927 are home to old stellar populations with a mean age of ∼3 Gyr (according to solar metallicity, single stellar population models of Bruzual & Charlot 2003). This corresponds to a formation redshift of $z_* \sim 3$ for the bulk of the stars in these galaxies. The values of the slope and scatter presented in this work were obtained using all passive members up to more than 0.5 Mpc from the center, without restricting ourselves to the central 40″ (diameter; ∼ 0.3 Mpc) as in Lidman et al. (2004), and are consistent with measurements in lower redshift clusters (Stanford et al. 1998).

Looking at morphology and colors, we do not see any indication of the existence of a population of S0 galaxies with a bluer (with respect to elliptical galaxies) color-magnitude sequence, in contrast to what has been observed in the galaxy cluster RDCS J0910+5422 at $z = 1.1$ (Mei et al. 2006a). As pointed out by Mei et al. (2006a), the existence of a bluer color-magnitude sequence of the S0 galaxies with respect to the elliptical galaxies in RDCS J0910+5422 could be the result of a still forming cluster, with these bluer S0 galaxies being part of a group infalling from the field onto a more evolved red cluster population. RDCS J1252.9−2927 presents a more evolved structure, having a more evolved early-type population, with elliptical and S0 galaxies distributed over a common red sequence.

From Figure 14, we observe that all spectroscopic members without detectable [O II] ($\lambda 3727$) emission have magnitudes brighter than $K_s = 21.5$, corresponding to ∼$K_s^* + 1.5$ ($K_{s,\mathrm{rest}}^* = -24$) at $z = 1.237$ (Strazzullo et al. 2006). This indicates the

TABLE 6
COLOR-MAGNITUDE FITTING

Fit No.	Slope	Color at $K_s = 18.5$	Intrinsic Scatter	Comments
1...............	-0.048 ± 0.015	1.85	0.070	Lidman et al. (2004)
2...............	-0.042 ± 0.022	1.87	0.061	This work

NOTE.—Only spectroscopic members without [O II] emission are used to fit the CM relation (solid red line in Fig. 14).
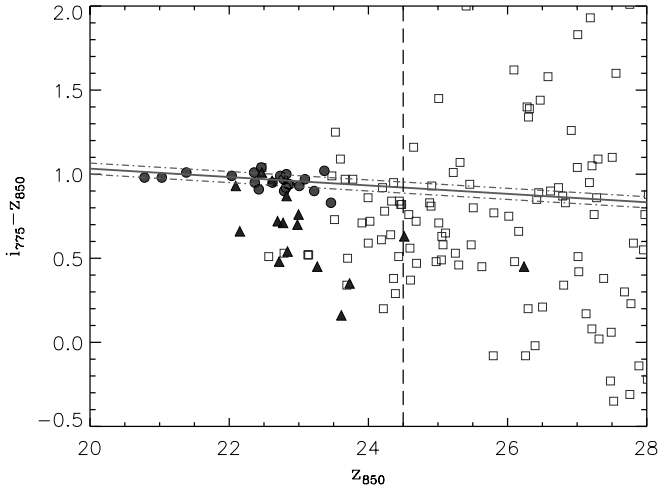
FIG. 15.— ACS color-magnitude diagram (CMD) of spectroscopic cluster members (*circles and triangles*) and photometric members (*squares*). Photometric redshifts are computed by using the Bayesian method (Benítez 2000; Benítez et al. 2004). Colors and magnitudes are computed in the AB system. Red circles correspond to passive members, while blue triangles correspond to [O II] emission-line galaxies. The best-fit color-magnitude relation and scatter from Blakeslee et al. (2003b) are shown in green. Only objects within the central 1 Mpc region around the cluster center and with $1.14 < z_{phot} < 1.34$ are shown. A color-magnitude relation for early-type galaxies is seen down to $z_{850} = 24.5$ (*dashed vertical line*). At fainter magnitudes this relation seems to be truncated in the bandpasses shown here, although this cutoff magnitude can be affected by uncertainties in the photometric redshifts. [*See the electronic edition of the Journal for a color version of this figure.*]

spectroscopic limit for galaxies with no detectable [O II] emission, while star-forming objects can be confirmed down to $K_s \sim 24$ ($\sim K_s^* + 4$). Star formation is active in faint ($>K_s^* + 1.5$), less massive objects with only a few star-forming members with $K_s < 21.5$. One of these objects is ID 174, the cluster member AGN, which is also the reddest ($J - K_s \sim 1.3$) member in Figure 14. The other star-forming galaxies (IDs 309, 339, 445 and 345) are well located within the near-IR CM relation.

If the fit of the cluster red sequence were restricted to cluster members brighter than $\sim K_s^*$, the resulting slope would be considerably flatter. This steepening of the slope when including fainter passive members could be due in part to the selection effect imposed by our inability to detect passive members below the spectroscopic limit of our survey. Star-forming objects, having bluer colors, would contribute to produce a fit slope steeper than the one obtained if only more luminous and passive (redder) objects were considered. The selection effect caused by the spectroscopic limit of passive galaxies prevent us from properly investigating the faint end of the red cluster sequence, in particular its buildup at this high redshift. As indicated by Tanaka et al. (2005), the faint end of the red cluster sequence seems to be still under construction at $z \sim 0.8$. The observed deficiency of galaxies at the faint end in $z \sim 0.8$ clusters suggests that part of the blue cluster galaxy population may well be the progenitors of the present-day faint-end population of the red sequence (De Lucia et al. 2004), as supported by recent high-resolution simulations (De Lucia et al. 2006), which, however, find it difficult to reproduce such tight color sequences at this redshift. More observations are needed to firmly establish this.

In Figure 15 we show the color-magnitude diagram using the ACS filters. Here we include spectroscopically confirmed passive (*red circles*) and emission-line (*blue triangles*) cluster members. Squares are objects with photometric redshifts (Benítez 2000) in the range $1.12 < z_{phot} < 1.35$ and within an aperture of
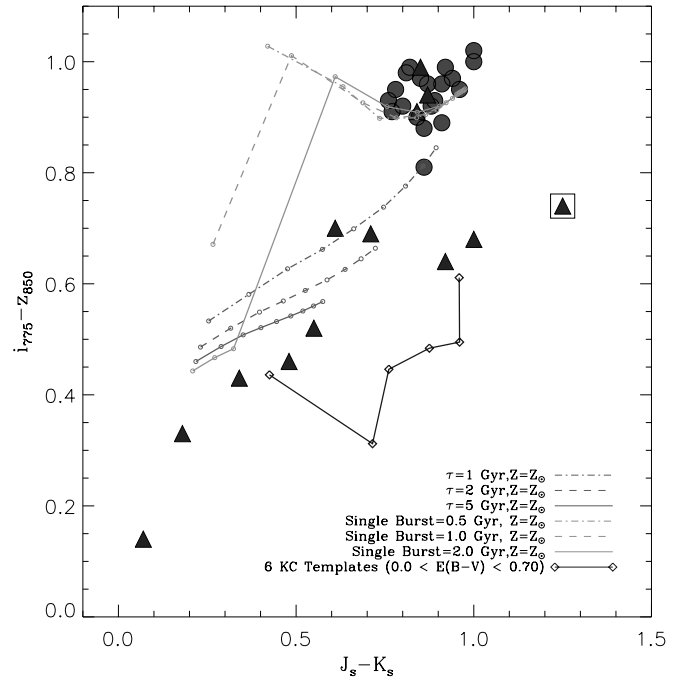

FIG. 16.— Distribution of spectroscopic cluster members in color-color space. All magnitudes are AB. Red filled circles correspond to passive galaxies, and blue filled triangles to [O II] emission galaxies. The open square indicates the only known AGN at the cluster redshift (ID 174). Model tracks are the same as those used in Fig. 2, spanning from 1 to 5 Gyr with intervals of 0.5 Gyr (see text). In this plot we show at the same time the color of passive and star-forming galaxies in both ACS and ISAAC filters. We note that this color-color diagram improves the selection of passive, red objects with respect to a $J - K$ color cut only. [*See the electronic edition of the Journal for a color version of this figure.*]

1 Mpc centered in the cluster (we excluded known spectroscopic nonmembers). These photometric redshifts have been corrected for a systematic deviation $\langle z_{spec} - z_{phot} \rangle = 0.17$. The red sequence can be traced down to a magnitude of $z_{850} = 24.5$ in these ACS bandpasses, vanishing quickly at fainter magnitudes. However, this cutoff magnitude can be affected by uncertainties in the photometric redshifts.

3.5. *Color-Color Distribution of Cluster Galaxies*

The distribution of spectroscopic cluster members in color-color space is shown in Figure 16. Red filled circles correspond to passive galaxies, and blue filled triangles to [O II] emission galaxies. The open square indicates the only known AGN at the cluster redshift (ID 174; see § 2.4). A clear separation between passive and star-forming galaxies is seen, with the exception of three emission-line galaxies, IDs 309, 345 and 445, which are located in the locus of passive members. These galaxies are also located in the red sequence of both $i_{775} - z_{850}$ versus z_{850} and $J_s - K_s$ versus K_s color-magnitude diagrams. The estimated SFR for these objects varies from 0.5 to 2.9 $M_\odot$ yr^{-1} (see Table 2), although the error bars are large.

The shape of the continuum and the [O II] ($\lambda 3727$) line of IDs 345 and 445 are consistent with their red ($i_{775} - z_{850} \sim 0.95$, $J_s - K_s \sim 0.8$) colors and star-forming nature. ID 309, on the other hand, shows a rather flat continuum up to 9000 Å, suggesting that we are looking at a dust-rich star-forming galaxy. The increase in number of sky lines, a relatively low S/N (~ 3), and therefore a poorer extraction of the continuum beyond 8500 Å, may have caused the flattening of the spectrum toward red wavelengths, in contrast to its red $i_{775} - z_{850}$ color. These galaxies are located within an annulus spanning from ~ 0.4 to ~ 0.8 Mpc in

radius from the two central bright elliptical galaxies, which corresponds to $R/R_{200} \simeq 0.43$–0.85 in Postman et al. (2005). The morphology-radius relation obtained for a composite cluster sample of seven galaxy clusters (including RDCS J1252.9−2927) at $z \sim 1$ observed with the ACS (Postman et al. 2005) shows that these objects are in a region where the average fraction of early-type galaxies (~39%) is about half that of late-type galaxies (~61%). Red, possibly obscured, star-forming galaxies in clusters at low redshift have already been reported in the literature (Duc et al. 2002; Coia et al. 2005; Wolf et al. 2005; Popesso et al. 2006), while similar objects have also been observed at redshift $z > 0.8$ (van Dokkum & Stanford 2003; Demarco et al. 2005) and in the field up to $z \sim 2$ (Franzetti et al. 2006).

Finally, we note that the two other [O II] galaxies with colors $J_s − K_s > 0.9$ (IDs 248 and 339), excluding the X-ray source ID 174, can be starburst galaxies with $E(B − V) > 0.39$ (Kinney et al. 1996), as shown in Figures 2 and 16, while the colors of the rest of the member star-forming galaxies can be reproduced by galaxies with $Z = Z_\odot$ and exponential SFRs (see Figs. 2 and 16). We also note that ID 339, with an elongated and irregular morphology, has a blue color in the optical ($i_{775} − z_{850} = 0.64$) but a red color in the near-IR ($J_s − K_s = 0.92$), suggesting that this star-forming galaxy has a significant amount of dust obscuring an important fraction of its "blue" light.

3.6. Morphologies and Spectrophotometric Properties

The morphological T-type class (de Vaucouleurs et al. 1976) as determined by Postman et al. (2005) for cluster members is given in Table 3. T-type values range from −5 for elliptical galaxies to 8 for disk/irregular galaxies. A value of −2 corresponds to S0 galaxies, values between −1 and 1 are assigned to morphologies between S0 and Sa, and a value of 6 corresponds to an Sd morphology. In general, we observe the well-known correlation between morphology and SFR. Most of the star-forming objects in this cluster have irregular morphologies or irregular disky structures where star formation is taking place. One of these, ID 6301, may be a possible merger with two compact bright regions surrounded by a gas envelope. Another one, ID 619, shows clear spiral-arm features and could also be a merger. In contrast, most of the passive galaxies have morphologies typical of elliptical and S0 galaxies, with no ongoing star formation due to their poor or zero gas content.

Passive early-type galaxies have red colors, while star-forming late-type galaxies are blue, (see Fig. 14), a manifestation of the well-known correlation between stellar populations and morphology. However, in Figure 14 we observe that a few star-forming galaxies have colors as red as the passive cluster members in the red sequence. One of these sources is ID 174, the confirmed cluster member X-ray source (see § 2.4), with a $J − K_s$ color about 0.35 mag redder than the average color of red sequence members and whose star formation could be due to the central, dust-obscured AGN. The other red, star-forming sources in the red sequence of Figure 14 are IDs 248, 309, 339, 345, and 445. While IDs 248 and 339 show an irregular disky appearance, IDs 309, 345, and 445 are characterized by a prominent central bulge surrounded by a diffuse disk structure (see Fig. Set 5). We observe that IDs 309, 345 and 445 also have red $i_{775} − z_{850}$ colors ($i_{775} − z_{850} \sim 0.95$) that locate them in the locus occupied by red, passive galaxies in Figure 16. While the star formation in these sources must be occurring in their gas-rich regions, their red colors should arise from the combined effect of old stellar populations and dust reddening. One interesting object is ID 726. This source is very compact and also shows a clear [O II] emission line in its spectrum, as shown in Figure 5.31. In addition, its blue color (see

Table 3) is consistent with the flat continuum of its spectrum. With a magnitude $M_B = −20.74$, this object can be considered in the class of luminous compact blue galaxies reported in the literature (e.g., Werk et al. 2004; Hammer et al. 2005; Noeske et al. 2006). This object has a very compact morphology (it is similar to the PSF), so Postman et al. did not provide a morphological T-type for it (see Table 3).

4. DISCUSSION AND CONCLUSIONS

We have combined an extensive multiwavelength data set to provide a comprehensive picture of the X-ray luminous, massive cluster of galaxies RDCS J1252.9−2927 at $z = 1.237$. ACS data provide detailed morphological information for galaxies, and accurate photometry. By using FORS on the VLT, we were able to spectroscopically confirm 38 cluster members. The overall projected distribution of spectroscopic cluster members presents a clear elongation in the east-west direction, consistent with the elongation observed in the gas (Rosati et al. 2004) and dark matter (Lombardi et al. 2005) distributions. As pointed out by Rosati et al. (2004), the X-ray surface brightness distribution of the core of RDCS J1252.9−2927 has a comet-like shape, resembling a cold front in low-redshift clusters (e.g., Mazzotta et al. 2001) produced by a merging process of a subclump in the east-west direction.

The velocity dispersion σ_v of the cluster members is 747^{+74}_{-84} km s^{-1}. Assuming virial equilibrium, we find that the virial mass is $\sim 5 \times 10^{14}$ $M_\odot$. Our mass estimates are also consistent with the mass estimates from the X-ray data (Rosati et al. 2004; Ettori et al. 2004) and the weak-lensing mass map (Lombardi et al. 2005). Our value of σ_v is also consistent with the L_X-σ_v relation for clusters, but turns out to be in disagreement with the σ_v-T_X relation (Xue & Wu 2000). While the observed L_X and T_X values follow the L_X-T_X relation of Xue & Wu (2000), the deviation from the σ_v-T_X relation may be the signature of a galaxy distribution still not in fully dynamical equilibrium.

Indeed, RDCS J1252.9−2927 has not yet attained an equilibrium state, as suggested by a more detailed analysis of the velocity distribution of cluster members. RDCS J1252.9−2927 is the most distant cluster for which a substructure analysis can be attempted. The kurtosis (Beers et al. 1991) indicates that the velocity distribution of cluster members is not Gaussian at the >95% c.l. The weighted gap procedure finds a significant gap in the space of ordered velocities, and a 3D KMM study detects substructure in velocity at the 95.6% c.l. The substructure is composed by two groups of galaxies which are mostly distributed in a east-west direction on the sky, as shown in Figure 11. Twenty-six galaxies are confirmed in the "low-velocity" group (centered at $−354 \pm 159$ km s^{-1} with respect to the cluster mean velocity), with a velocity dispersion of 486^{+47}_{-85} km s^{-1} and located mostly to the west of the cluster center. Twelve galaxies are confirmed in the "high-velocity" group (centered at 845 ± 182 km s^{-1} with respect to the cluster mean velocity), with a velocity dispersion of 426^{+57}_{-105} km s^{-1} and located mostly to the east of the cluster center.

The existence of the above correlations between positions and velocities of cluster galaxies is a footprint of real substructure. In particular, it suggests that RDCS J1252.9−2927 is forming via a merger along the east-west direction. Going further, we estimate the mass contained within R_{200} for each group (see § 3.2). The sum of these two masses is about half of the cluster mass, and should be considered as a lower limit of the cluster mass. These groups may be the virialized cores of two larger systems, with possibly $R \gtrsim 2R_{200}$ and larger velocity dispersions. The fact that the X-ray emission presents a single peak, although elongated in morphology, indicates that these two groups have already started

virialization. This is supported by the degree of merging of the group members as shown in Figure 11. Our substructure analysis has thus found the remnant traces of two subclusters merging parallel to the sky, as suggested by the lack of a clear bimodal distribution of the overall cluster velocity field.

By using the σ_v-T_X relation for groups in Xue & Wu (2000), we find that both groups have velocity dispersions consistent with the same temperature of ∼2 keV. This temperature is inconsistent with the overall cluster temperature of ∼6 keV, yet it corresponds to about half the total cluster X-ray luminosity according to the group L_X-T_X relation (Xue & Wu 2000). Thus, both groups seem to be independently virialized, and the sum of their X-ray luminosities would be approximately equal to the total cluster L_X. The temperature value of the overall ICM would have been the consequence of gas particle interactions at an earlier epoch during the merger of the groups. By the epoch of observation, the overall ICM is consistent with being in an almost isothermal hydrostatic equilibrium in a single potential well, while the groups are fossilized in the velocity dispersion substructure. The agreement of the observed cluster L_X and T_X values with the L_X-T_X relation and the deviation of the cluster values from the σ_v-T_X relation show that the gas in the cluster is more relaxed than the galaxies. Since galaxies behave more like dark matter particles, they still need more time to reach the σ_v-T_X relation expected for the cluster. In summary, the elongated shape of the cluster structure (in all its components, baryons and dark matter) and the substructure in velocity leads us to conclude that RDCS J1252.9−2927 has not yet reached a final virial state; we may be seeing gravitational collapse of two or more subclusters along a high-density filament.

In this work we present an improved analysis of the near-IR color-magnitude diagram of galaxies in RDCS J1252.9−2927, based on ISAAC data that have been reprocessed in order to optimize image quality and obtain more accurate photometry over the entire region covered by near-IR observations. We use only spectroscopic cluster members, and the analysis extends over more than 1 Mpc from the cluster center, in contrast to previous studies. The fit to the red cluster sequence, including all passive spectroscopic members, yields slope and scatter values consistent with the result of Blakeslee et al. (2003b) and Lidman et al. (2004). This indicates that the early-type galaxy cluster population has formed most of its stellar content at $z \sim 3$ and has passively evolved since down to the epoch of observation, as previously shown for $z \sim 1$ clusters (van Dokkum & Stanford 2003; Blakeslee et al. 2003b, 2006; Lidman et al. 2004; Mei et al. 2006a, 2006b). If we restrict the fit of the cluster red sequence to spectroscopic members brighter than ∼K_s^*, the slope becomes significantly shallower, suggesting that the CM relation of passively evolving systems may be nonlinear, although this could also be due to a selection effect. The [O II] emission line observed in 17 cluster galaxies allows us to estimate a lower limit value of $0.7\ M_\odot\ \mathrm{yr}^{-1}$ for the median SFR in the cluster. Only 5 out of 25 spectroscopic members that are brighter than $K_s^* + 1.5$ show ongoing star formation. Three star-forming galaxies have colors as red as galaxies in the red cluster sequence of both $i_{775} - z_{850}$ versus z_{850} (optical) and $J_s - K_s$ versus K_s (near-IR) color-magnitude diagrams. One additional star-forming galaxy is observed in the red sequence of the near-IR color-magnitude diagram, but not in the optical one, suggesting that we are observing a dust-rich galaxy. Finally, a highly obscured AGN is observed to be a spectroscopic member of RDCS J1252.9−2927, and we do not find any evidence of "red mergers" like those observed in the galaxy cluster MS 1054 (van Dokkum et al. 1999).

The projected distribution of passive and star-forming galaxies in this cluster shows a spectrum-density relation that qualitatively resembles the observed morphology-density relation at $z \sim 1$ (Smith et al. 2005; Postman et al. 2005): passive, early-type galaxies dominate the cluster core, while star-forming, late-type galaxies are found in the outskirts of the cluster. From a dynamical point of view, we are witnessing hierarchical structure formation: we are observing a merger of two large groups of galaxies into a more massive structure.

REFERENCES

Appenzeller, I., & Rupprecht, G. 1992, ESO Messenger, March, 18
Ashman, K. M., Bird, C. M., & Zepf, S. E. 1994, AJ, 108, 2348
Balogh, M. L., Schade, D., Morris, S. L., Yee, H. K. C., Carlberg, R. G., & Ellingson, E. 1998, ApJ, 504, L75
Bardelli, S., Zucca, E., Vettolani, G., Zamorani, G., Scaramella, R., Collins, C. A., & MacGillivray, H. T. 1994, MNRAS, 267, 665
Beers, T. C., Flynn, K., & Gebhardt, K. 1990, AJ, 100, 32
Beers, T. C., Gebhardt, K., Forman, W., Huchra, J. P., & Jones, C. 1991, AJ, 102, 1581
Benítez, N. 2000, ApJ, 536, 571
Benítez, N., et al. 2004, ApJS, 150, 1
Bird, C. M., & Beers, T. C. 1993, AJ, 105, 1596
Blakeslee, J. P., et al. 2003a, ApJ, 589, 693
———. 2003b, ApJ, 596, L143
———. 2006, ApJ, 644, 30
Brodwin, M., et al. 2006, ApJ, 651, 791
Bruzual, G., & Charlot, S. 2003, MNRAS, 344, 1000
Bullock, J. S., Kolatt, T. S., Sigad, Y., Somerville, R. S., Kravtsov, A. V., Klypin, A. A., Primack, J. R., & Dekel, A. 2001, MNRAS, 321, 559
Calzetti, D., et al. 2005, ApJ, 633, 871
Carlberg, R. G., Yee, H. K. C., & Ellingson, E. 1997, ApJ, 478, 462
Carpenter, J. M. 2001, AJ, 121, 2851
Charlot, S., & Longhetti, M. 2001, MNRAS, 323, 887
Cohen, M., Wheaton, W. A., & Megeath, S. T. 2003, AJ, 126, 1090

Coia, D., et al. 2005, A&A, 431, 433
Danese, L., de Zotti, G., & di Tullio, G. 1980, A&A, 82, 322
De Lucia, G., Springel, V., White, S. D. M., Croton, D., & Kauffmann, G. 2006, MNRAS, 366, 499
De Lucia, G., et al. 2004, ApJ, 610, L77
Demarco, R., et al. 2005, A&A, 432, 381
de Vaucouleurs, G., de Vaucouleurs, A., & Corwin, H. G. 1976, University of Texas Monographs in Astronomy (Austin: Univ. Texas Press)
Doherty, M., et al. 2004, MNRAS, 354, L7
Dolag, K., Bartelmann, M., Perrotta, F., Baccigalupi, C., Moscardini, L., Meneghetti, M., & Tormen, G. 2004, A&A, 416, 853
Dressler, A. 1980, ApJ, 236, 351
Dressler, A., Smail, I., Poggianti, B. M., Butcher, H., Couch, W. J., Ellis, R. S., & Oemler, A. J. 1999, ApJS, 122, 51
Dressler, A., et al. 1997, ApJ, 490, 577
Duc, P.-A., et al. 2002, A&A, 382, 60
Ellingson, E., & Yee, H. K. C. 1994, ApJS, 92, 33
Elston, R. J., et al. 2006, ApJ, 639, 816
Ettori, S., Tozzi, P., Borgani, S., & Rosati, P. 2004, A&A, 417, 13
Fadda, D., Girardi, M., Giuricin, G., Mardirossian, F., & Mezzetti, M. 1996, ApJ, 473, 670
Fasano, G., & Franceschini, A. 1987, MNRAS, 225, 155
Finn, R. A., et al. 2005, ApJ, 630, 206
Ford, H. C., et al. 1998, Proc. SPIE, 3356, 234

Franzetti, P., et al. 2006, preprint (astro-ph/0607075)

Gebhardt, K., & Beers, T. C. 1991, ApJ, 383, 72

Gioia, I. M., Braito, V., Branchesi, M., Della Ceca, R., Maccacaro, T., & Tran, K.-V. 2004, A&A, 419, 517

Gioia, I. M., Henry, J. P., Mullis, C. R., Ebeling, H., & Wolter, A. 1999, AJ, 117, 2608

Girardi, M., Demarco, R., Rosati, P., & Borgani, S. 2005, A&A, 442, 29

Girardi, M., Fadda, D., Giuricin, G., Mardirossian, F., Mezzetti, M., & Biviano, A. 1996, ApJ, 457, 61

Girardi, M., Giuricin, G., Mardirossian, F., Mezzetti, M., & Boschin, W. 1998, ApJ, 505, 74

Girardi, M., & Mezzetti, M. 2001, ApJ, 548, 79

Glazebrook, K., Blake, C., Economou, F., Lilly, S., & Colless, M. 1999, MNRAS, 306, 843

Hammer, F., Flores, H., Elbaz, D., Zheng, X. Z., Liang, Y. C., & Cesarsky, C. 2005, A&A, 430, 115

Hashimoto, Y., Barcons, X., Böhringer, H., Fabian, A. C., Hasinger, G., Mainieri, V., & Brunner, H. 2004, A&A, 417, 819

Helsdon, S. F., & Ponman, T. J. 2003, MNRAS, 339, L29

Holden, B. P., Stanford, S. A., Eisenhardt, P., & Dickinson, M. 2004, AJ, 127, 2484

Holden, B. P., et al. 2005, ApJ, 620, L83

Homeier, N. L., et al. 2005, ApJ, 621, 651

———. 2006a, AJ, 131, 143

———. 2006b, ApJ, 647, 256

Jansen, R. A., Franx, M., Fabricant, D., & Caldwell, N. 2000, ApJS, 126, 271

Jeltema, T. E., Canizares, C. R., Bautz, M. W., Malm, M. R., Donahue, M., & Garmire, G. P. 2001, ApJ, 562, 124

Kauffmann, G., White, S. D. M., Heckman, T. M., Ménard, B., Brinchmann, J., Charlot, S., Tremonti, C., & Brinkmann, J. 2004, MNRAS, 353, 713

Kewley, L. J., Geller, M. J., & Jansen, R. A. 2004, AJ, 127, 2002

Kewley, L. J., Geller, M. J., Jansen, R. A., & Dopita, M. A. 2002, AJ, 124, 3135

Kinney, A. L., Calzetti, D., Bohlin, R. C., McQuade, K., Storchi-Bergmann, T., & Schmitt, H. R. 1996, ApJ, 467, 38

Lidman, C., Rosati, P., Demarco, R., Nonino, M., Mainieri, V., Stanford, S. A., & Toft, S. 2004, A&A, 416, 829

Limber, D. N., & Mathews, W. G. 1960, ApJ, 132, 286

Lombardi, M., et al. 2005, ApJ, 623, 42

Malumuth, E. M., Kriss, G. A., Dixon, W. V. D., Ferguson, H. C., & Ritchie, C. 1992, AJ, 104, 495

Martel, A. R., Menanteau, F., Tozzi, P., Ford, H. C., & Infante, L. 2007, ApJS, 168, 19

Maughan, B. J., Jones, L. R., Ebeling, H., Perlman, E., Rosati, P., Frye, C., & Mullis, C. R. 2003, ApJ, 587, 589

Maughan, B. J., Jones, L. R., Ebeling, H., & Scharf, C. 2004, MNRAS, 351, 1193

Mazzotta, P., Markevitch, M., Vikhlinin, A., Forman, W. R., David, L. P., & VanSpeybroeck, L. 2001, ApJ, 555, 205

Mei, S., et al. 2006a, ApJ, 639, 81

———. 2006b, ApJ, 644, 759

Moorwood, A., Cuby, J.-G., & Lidman, C. 1998, ESO Messenger, 91, 9

Moorwood, A., et al. 1999, Messenger, 95, 1

Mullis, C. R., Rosati, P., Lamer, G., Böhringer, H., Schwope, A., Schuecker, P., & Fassbender, R. 2005, ApJ, 623, L85

Navarro, J. F., Frenk, C. S., & White, S. D. M. 1997, ApJ, 490, 493

Noeske, K. G., Koo, D. C., Phillips, A. C., Willmer, C. N. A., Melbourne, J., Gil de Paz, A., & Papaderos, P. 2006, ApJ, 640, L143

Oke, J. B. 1974, ApJS, 27, 21

Pinkney, J., Roettiger, K., Burns, J. O., & Bird, C. M. 1996, ApJS, 104, 1

Pisani, A. 1993, MNRAS, 265, 706

———. 1996, MNRAS, 278, 697

Popesso, P., Biviano, A., Romaniello, M., Böhringer, H. 2006, preprint (astro-ph/0609080)

Postman, M., et al. 2005, ApJ, 623, 721

Press, W. H., Teukolsky, S. A., Vetterling, W. T., & Flannery, B. P. 1992, Numerical Recipes in Fortran (Cambridge: Cambridge Univ. Press)

Quintana, H., Carrasco, E. R., & Reisenegger, A. 2000, AJ, 120, 511

Rettura, A., et al. 2006, A&A, 458, 717

Rosati, P. 2004, Clusters of Galaxies: Probes of Cosmological Structure and Galaxy Evolution, ed. J. S. Mulchaey, A. Dressler, & A. Oemler (Cambridge: Cambridge Univ. Press), 72

Rosati, P., della Ceca, R., Norman, C., & Giacconi, R. 1998, ApJ, 492, L21

Rosati, P., Stanford, S. A., Eisenhardt, P. R., Elston, R., Spinrad, H., Stern, D., & Dey, A. 1999, AJ, 118, 76

Rosati, P., et al. 2004, AJ, 127, 230

Schlegel, D. J., Finkbeiner, D. P., & Davis, M. 1998, ApJ, 500, 525

Smith, G. P., Treu, T., Ellis, R. S., Moran, S. M., & Dressler, A. 2005, ApJ, 620, 78

Stanford, S. A., Eisenhardt, P. R., & Dickinson, M. 1998, ApJ, 492, 461

Stanford, S. A., Elston, R., Eisenhardt, P. R., Spinrad, H., Stern, D., & Dey, A. 1997, AJ, 114, 2232

Stanford, S. A., Holden, B., Rosati, P., Eisenhardt, P. R., Stern, D., Squires, G., & Spinrad, H. 2002, AJ, 123, 619

Stanford, S. A., et al. 2005, ApJ, 634, L129

———. 2006, ApJ, 646, L13

Strazzullo, V., et al. 2006, A&A, 450, 909

Tanaka, M., Kodama, T., Arimoto, N., Okamura, S., Umetsu, K., Shimasaku, K., Tanaka, I., & Yamada, T. 2005, MNRAS, 362, 268

Tanaka, M., Kodama, T., Arimoto, N., & Tanaka, I. 2006, MNRAS, 365, 1392

Taylor, J. R. 1997, Introduction to Error Analysis (2nd ed.; Mill Valley: University Science Books)

The, L. S., & White, S. D. M. 1986, AJ, 92, 1248

Thomas, T., & Katgert, P. 2006, A&A, 446, 31

Toft, S., Mainieri, V., Rosati, P., Lidman, C., Demarco, R., Nonino, M., & Stanford, S. A. 2004, A&A, 422, 29

Tonry, J., & Davis, M. 1979, AJ, 84, 1511

Tran, K.-V. H., Franx, M., Illingworth, G., Kelson, D. D., & van Dokkum, P. 2003, ApJ, 599, 865

Treu, T., et al. 2005, ApJ, 633, 174

van der Wel, A., Franx, M., van Dokkum, P. G., Rix, H.-W., Illingworth, G. D., & Rosati, P. 2005, ApJ, 631, 145

van Dokkum, P. G., Franx, M., Fabricant, D., Kelson, D. D., & Illingworth, G. D. 1999, ApJ, 520, L95

van Dokkum, P. G., & Stanford, S. A. 2003, ApJ, 585, 78

van Dokkum, P. G., & van der Marel, R. P. 2006, peprint (astro-ph/0609587)

Wainer, H., & Schacht, S. 1978, Psychometrika, 43, 203

Wake, D. A., Collins, C. A., Nichol, R. C., Jones, L. R., & Burke, D. J. 2005, ApJ, 627, 186

Werk, J. K., Jangren, A., & Salzer, J. J. 2004, ApJ, 617, 1004

Wolf, C., Gray, M. E., & Meisenheimer, K. 2005, A&A, 443, 435

Xue, Y.-J., & Wu, X.-P. 2000, ApJ, 538, 65